Enhancing Structural Control in Covalent Organic Frameworks through Steric Interaction-Driven Linker Design

Alena Winter,[a] Farzad Hamdi,[b,c,d] Andreas Eichhöfer,[e] Kay Saalwächter,[f] Panagiotis Kastritis,[b,c,d,g] Frederik Haase[a,h]*

[a] Institute of Chemistry, Faculty of Natural Sciences II, Martin-Luther-Universität Halle-Wittenberg, von-Danckelmann-Platz 4, Halle/Saale, Germany
[b] Interdisciplinary Research Center HALOmem, Charles Tanford Protein Center, Martin Luther University Halle-Wittenberg, Kurt-Mothes-Straße 3a, Halle/Saale, Germany
[c] Institute of Biochemistry and Biotechnology, Martin Luther University Halle-Wittenberg, Kurt-Mothes-Straße 3, Halle/Saale, Germany
[d] Biozentrum, Martin Luther University Halle-Wittenberg, Weinbergweg 22, Halle/Saale, Germany
[e] Institute for Nanotechnology (INT), Karlsruhe Institute of Technology (KIT), Hermann-von-Helmholtz-Platz 1, Eggenstein-Leopoldshafen, Germany
[f] Institute of Physics, Martin-Luther-Universität Halle-Wittenberg, Betty-Heimann-Str. 7, Halle/Saale, Germany
[g] Institute of Chemical Biology, National Hellenic Research Foundation, Athens, Greece
[h] Institute of functional Interfaces (IFG), Karlsruhe Institute of Technology (KIT), Hermann-von-Helmholtz-Platz 1, Eggenstein-Leopoldshafen, Germany
* correspondence address: frederik.haase@chemie.uni-halle.de

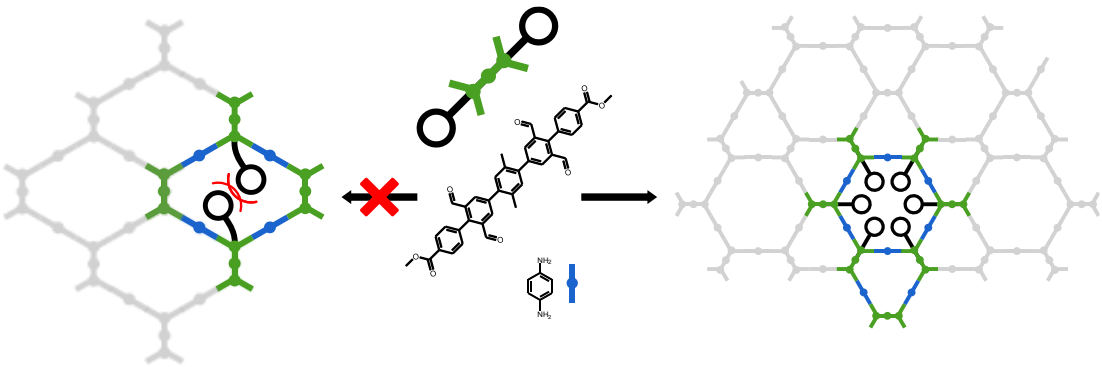

Abstract

Covalent Organic Frameworks (COFs) exhibiting kagome (*kgm*) structures are promising crystalline porous materials with two distinct pores. However, the challenge arises from the potential formation of the polymorphic square-lattice (*sql*) structure, which is undesired in some cases. To this, we introduce a novel linker design strategy featuring bulky functional groups, enforcing the preferred *kgm* structure, while hindering *sql* network formation. Implementing this design, we synthesized a terphenyl core-based tetraaldehyde linker (4A2E) incorporating a bulky methoxycarbonyl-terminated phenyl group. By varying the diamine linker lengths, using phenylenediamine (PDA) and benzidine (Bz), the steric interaction was tuned leading to the formation of different topologies. Structural analysis revealed the formation of a *kgm* network formation with an unusual ABC stacking for the 4A2E-PDA-COF with the short PDA linker, in contrast to the *sql* network in 4A2E-Bz-COF with the longer benzidine. This steric interaction-driven design enhances control over COF structures, expanding the design toolbox, but also provides valuable insights into network formation and polymorphism.

Introduction

The appeal of covalent organic frameworks (COFs), and reticular materials in general, stems from their predictable structures, where the geometry of the building blocks determines the resulting net. However, with certain building block geometries, the outcome of a synthesis cannot always be predicted due to polymorphism. In three dimensional MOFs and COFs,[1–3] a significant challenge arises

from the vast array of potential structures (and nets) that can emerge from a single type of building block. In two-dimensional COFs, net polymorphism is mostly known from the competition between kagome (*kgm*) vs. square lattice (*sql*) when using planar four connected (4-c) linkers. Notable further examples of (pseudo-) polymorphism are frustrated COFs based on three connected (3-c) with a 4-c linker leading to sub-stochiometric 2D COFs.[4–6]

The competition of *kgm* vs. *sql* nets occurs as 4-c building blocks with angles of 60° and 120° between the functional groups can construct both nets without distorting the building blocks.[7,8] The *kgm* topology has generated much interest because it contains two differently-sized pores in one structure.[9] Targeting just one of these nets remains an unresolved challenge in COFs. Efforts have been undertaken to control the topology using different linkers. For example, by controlling the planarity of the building block[10] or with a hydrogen-bonding stabilized imine.[11] In many individual examples, tetraphenylethylene-based building blocks prefer to form the *kgm* structure,[7,8,12,13] while pyrene-based linkers prefer to form *sql* nets.[14–18] In these examples, it is often not clear, why the system prefers either *kgm* or *sql* structures. The different topologies based on the same linker have also been realized with different synthesis conditions.[1,19,20] However, only on very few systems, this synthetic control was possible.[21] Theoretic simulations have predicted that depending on the concentration and interaction of the solvent with the monomer, the nucleation of either *kgm* or *sql* should be possible.[22]

A much more well-understood type of polymorphism in 2D COFs is the so-called stacking modes, which describe the offset and sequence of layers. For structure elucidation, the stacking is often considered without disorder.[23] Stacking modes can be differentiated by the offset between different layers. When the layers have no offset vector (0Å offset), the stacking mode is referred to as eclipsed (i.e. AA stacking sequence,). However, this idealized stacking is often assumed due to averaging of random offset stacking[24] and is only rarely observed in reality.[13] Alternately, uniform slipping of the layers in one direction (1-2Å offset) can be observed.[25] If the backbone of the COF is positioned over the center of the pore in the layer below, the stacking is called staggered or AB/ABC stacked.[26] Eclipsed and slipped stacking has important implications for the electronic properties of the material,[26] which can be experimentally controlled by the addition of side chains,[27] using donor-acceptor strategies,[25,28,29] or introducing additional interactions between the layers.[30] Staggered stacking is a strategy for generating small pore COFs, which is an important feature for porous materials in gas separation.[31] Yet, only very few examples of staggered hexagonal honeycomb (*hcb*) COFs have been reported, where the stacking can be controlled, such as through tuning steric interactions between the layers[32], addition of a modulator[33] or synthesis conditions[34]. Despite this apparent control over the stacking, the ABC stacking mode in other nets is exceedingly rare. For example, to the best of our knowledge, it has only been reported once for the kagome dual (*kgd*)[35] and *kgm*[36] topology.

In this study, we investigated how steric interactions through the pores of 2D COFs affect their nets. We achieved the through-pore interactions by rigid attachment of a long and bulky methoxycarbonyl-terminated phenyl group to a tetraaldehyde linker. Using this modified tetraaldehyde, we synthesized COFs with different linear diamine linkers. We observed a *kgm* structure with the short *p*-phenylenediamine and a *sql* structure with the longer benzidine (*p*-diaminodiphenyl). Our work tackles the challenge of controlling the nets with this sterically demanding linker design. The structural characterization by powder X-ray diffraction (PXRD) and transmission electron microscopy (TEM) confirmed the selectivity for *sql* and *kgm*. Additionally, we found evidence for the rare ABC stacking in the *kgm* COF. Force field simulations provided evidence for strong steric crowding in the rhombic pore of a hypothetical *sql* 4A2E-PDA-COF, based on the *p*-phenylenediamine, that is relieved when forming the hexagonal pores in the *kgm* net. The longer benzidine linker increases the intrapore distance and decreases the steric demand, thus allowing the formation of a *sql* net. Our linker design enables

sterically demanding functional groups to control the net. This design principle expands the COF synthesis toolbox for inducing the *kgm* net more reliably.

Results

We designed a tetraaldehyde linker (4A2E, Figure 1 center) based on a terphenyl core with 2 aldehydes attached to each outer phenyl ring. The aldehydes are attached in 3 and 5 positions to form a 60° and a 120° bite angle between them, which allows the formation of both *kgm* and *sql* networks. The linker core was functionalized in the 60° bay with methyl groups to increase the solubility and the 120° bay was functionalized with bulky methyl benzoate moieties. The linker 4A2E was synthesized in a three-step synthesis starting from 2-Bromoisopthalaldehyde (for details see supplementary method section).

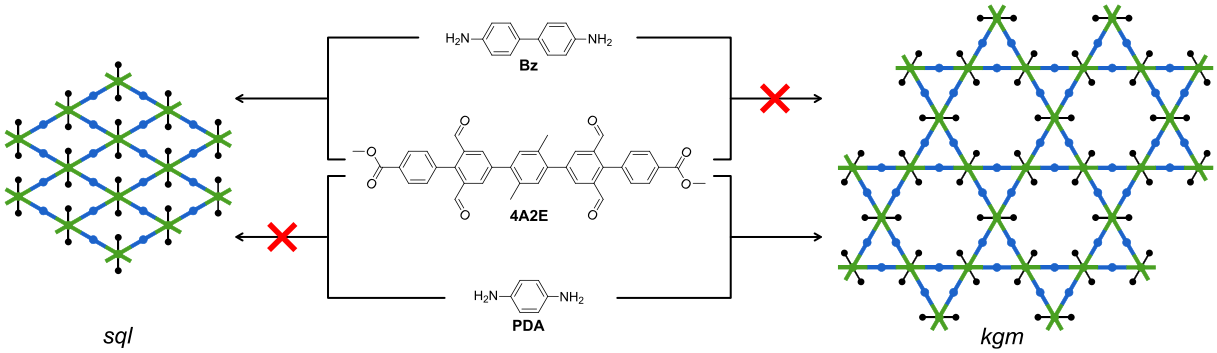

Figure 1: Schematic depiction of the possible formed nets (sql, left and kgm, right)

We employed the 4A2E linker for the synthesis of imine-based COFs using either phenylenediamine (PDA) or benzidine (Bz). The synthesis was performed as a solvothermal approach in a mixture of 1,4-dioxane and mesitylene, with trifluoroacetic acid (TFA) serving as the catalyst. After the reaction, the precipitated COFs were filtered off and washed thoroughly with methanol, followed by Soxhlet extraction with methanol and activation by using supercritical CO_2. After extensive screening of the solvent ratios and acid concentrations, we obtained two crystalline COFs 4A2E-PDA-COF and 4A2E-BZ-COF, using PDA and BZ as linear diamines, respectively.

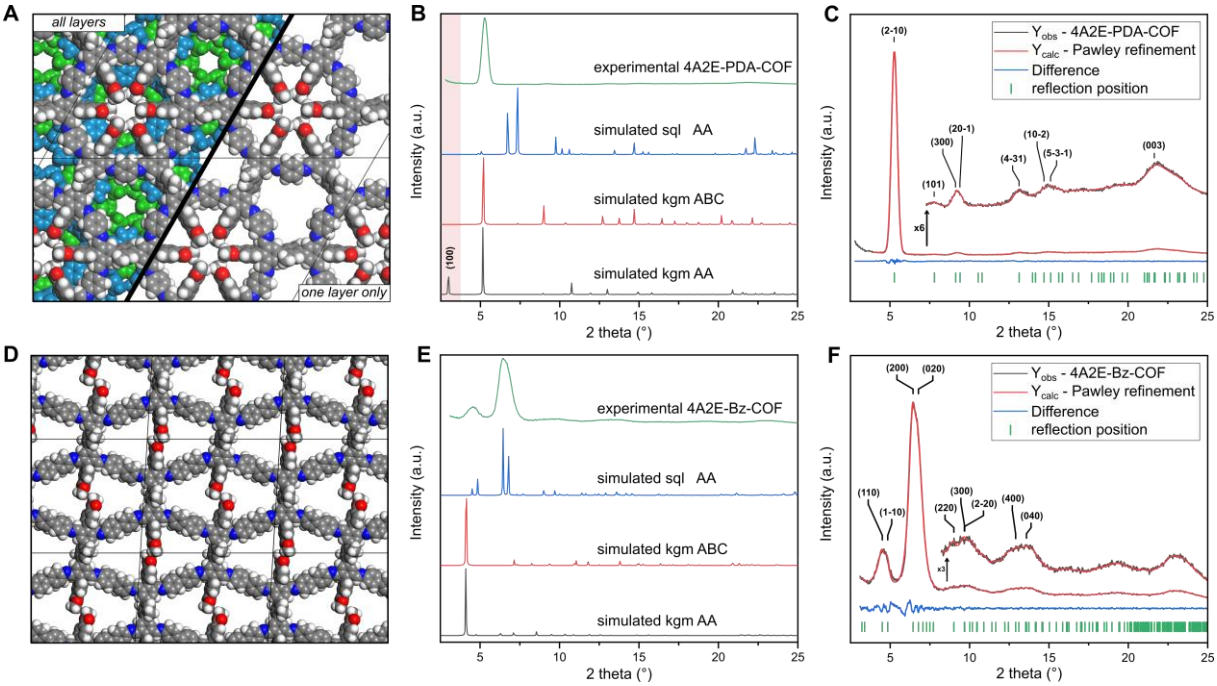

Figure 2: Simulated structures of 4A2E-PDA-COF (A) and 4A2E-Bz-COF (D), Experimental PXRD compared to the simulated patterns (B, E) and Pawley refinement of the PXRD patterns (C, F).

To verify the crystallinity of the 4A2E-PDA-COF, we performed PXRD. The diffractogram showed sharp reflexes with the most intense reflex at 5.22° 2θ, with additional less intense reflexes at 7.66°, 9.14°, 12.98°, 14.80°, and 21.40° (, B). As the linker geometry of 4A2E leads to two possible 2D nets, *sql* and *kgm*, we constructed structural models of both nets in AA eclipsed stacking in Materials Studio. Based on these models, we simulated PXRD patterns (Figure 2, B). The simulated *sql* structure pattern clearly does not match the observed PXRD of 4A2E-PDA-COF, as it showed intense reflections at 6.73° and 7.34° which do not match with the experimentally observed reflections, while the reflection at 5.22° is missing in the simulated pattern. Surprisingly, the simulated PXRD based on the *kgm* structural model with a $P\overline{3}$ symmetry and eclipsed stacking did not show a good fit either: while some of the reflections match, others are evidently missing. The most intense observed reflection at 5.16° matches well with the 110 reflection of the simulated structure, while the reflection at 10.77° can be explained by the 300 reflection. But crucially, the 100 reflection, predicted by the simulation at 2.98°, is completely absent in the experimentally observed pattern (Figure 2 B) even when measured at small angles (Figure S 12), while the observed reflection at 7.66° is absent in the simulated *kgm* pattern. This led us to believe that the *kgm* structural model with eclipsed stacking does not describe the structure accurately.

To gain additional orthogonal information about the crystal structure required for solving the COF's structure, we performed cryo-TEM. In the TEM the **4A2E**-PDA-COF showed intergrown crystallites ranging in size from 100 to 150 nm (Figure S 8), which rendered single crystal electron diffraction structure determination unfeasible. However, owing to the high resolution achieved in the TEM images, we could observe these crystallites in various orientations, including alignment with the [001] direction, clearly revealing the hexagonal symmetry of the structure (Figure 3 B, C). This observation confirmed a d-spacing of 16.9 Å in the fast Fourier transform (FFT) of the TEM images, matching well with the reflection observed in the PXRD at 5.22°, which can be assigned to the 110 reflection in a *kgm* model (Figure 2). Additionally, FFT and real space images showed no indications of a 100 reflection, anywhere in the TEM images of the **4A2E**-COF (Figure 3 C). This corresponds to the absence of this feature in the PXRD. The observed periodicities in the TEM, coupled with the hexagonal symmetry, evidently deviate from a simple eclipsed *kgm* model.

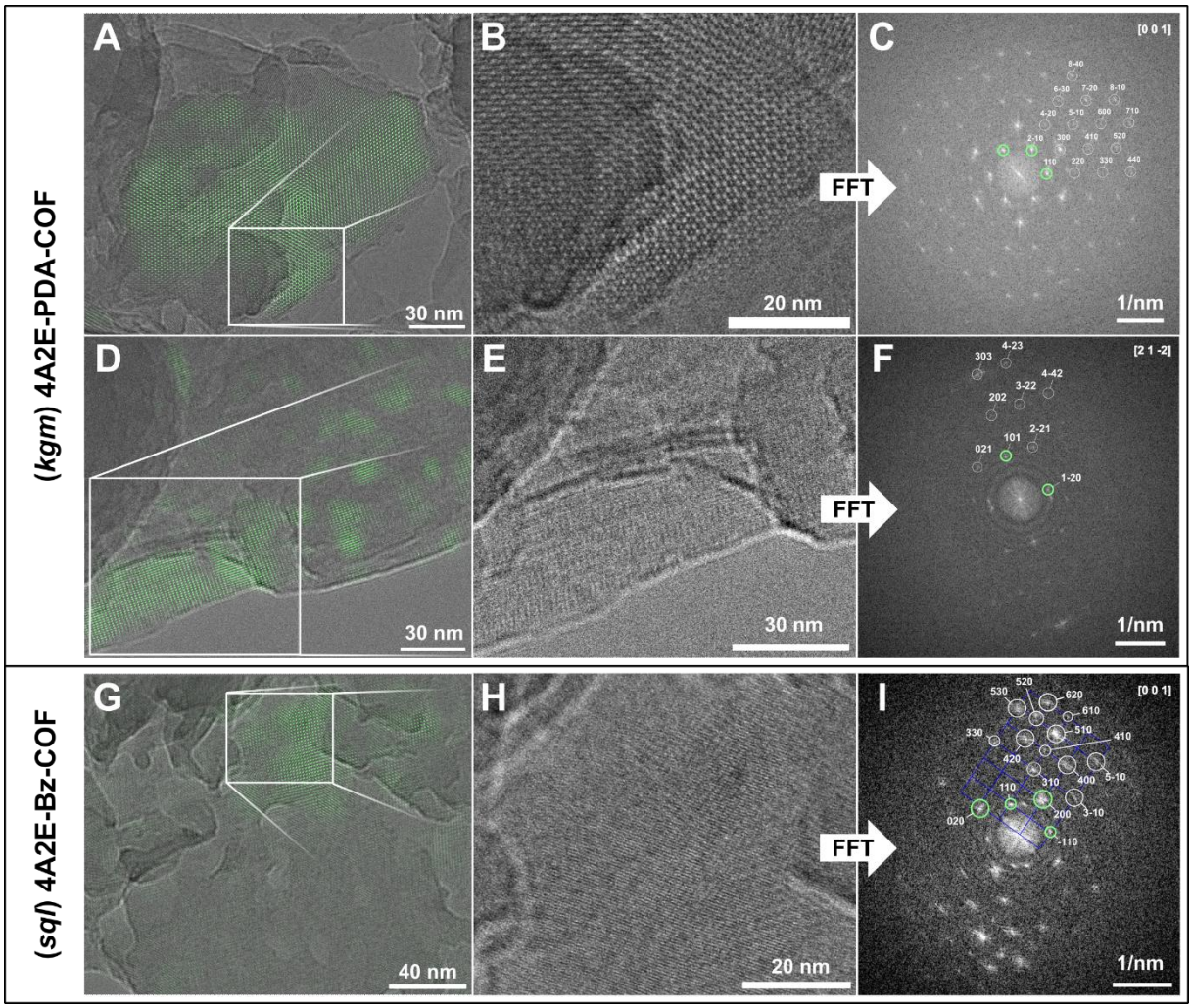

Figure 3: cryo-TEM images of the **4A2E**-PDA-COF (A-B, D-E) and the **4A2E**-Bz-COF (G-H) and the corresponding FFT images (C, F, I). The green overlays in A, D, G were generated by the Fourier filtering indicated in green in the corresponding FFT images (C, F, I).

Next, we intended to exclude sub-stoichiometric structures, as these can lead to unexpected unit cells and can appear under specific synthesis conditions or when competing interactions are at play in the structure formation.[4,37,38] When comparing the IR spectra of the **4A2E**-linker molecules and the **4A2E**-PDA-COF (Figure S 6), the strong band corresponding to the C=O stretching of the aldehyde at 1681 cm^{-1} disappears for the formed **4A2E**-PDA-COF, while the C=O stretch vibration of the methyl ester group only shifts slightly from 1715 cm^{-1} to 1733 cm^{-1} for the linker and the COF, respectively. At the same time a vibration at 1612 cm^{-1} appears that can be assigned to the imine C=N stretch vibration.[39] The characteristic amine vibrations from N-H stretch vibrations in the region 3100-3500 cm that are visible in the PDA linker completely disappear upon the formation of the **4A2E**-PDA-COF.

The stochiometric nature of the **4A2E**-PDA-COF was also verified by solid-state NMR (ssNMR) (Figure 4, B, including assignments following ref [39]), where no significant aldehyde peak was observed at 190 ppm. At the same time ssNMR showed the characteristic peak of the quaternary carbon of the methyl ester (**1**) at 165 ppm and the methyl ester carbon (**5**) can be assigned to the peak at 50 ppm for the **4A2E**-PDA-COF. The methyl ester peak is thus shifted downfield from the methyl group attached to the **4A2E** linker core, which can be found at 18 ppm. These measurements strongly indicate a stoichiometric structure as there are no dangling aldehyde groups or amine groups are detectable, and an intact methyl ester group. Additionally, dangling amines from a PDA core would not lead to the

formation of a two-periodic structure and would unlikely, but has been observed before under special cirumstances.[40]

To determine the porosity of the synthesized COFs, nitrogen sorption isotherms were measured at 77 K. The N_2 gas adsorption isotherms showed a type I isotherm with expected steep uptake at low pressures (Figure 4), as even the "larger" trigonal pores in a *kgm* net are below 1.4 nm as seen from the structure simulations. The resulting BET surface showed a moderate area of 622 m^2/g, which suggest an overall porous structure.

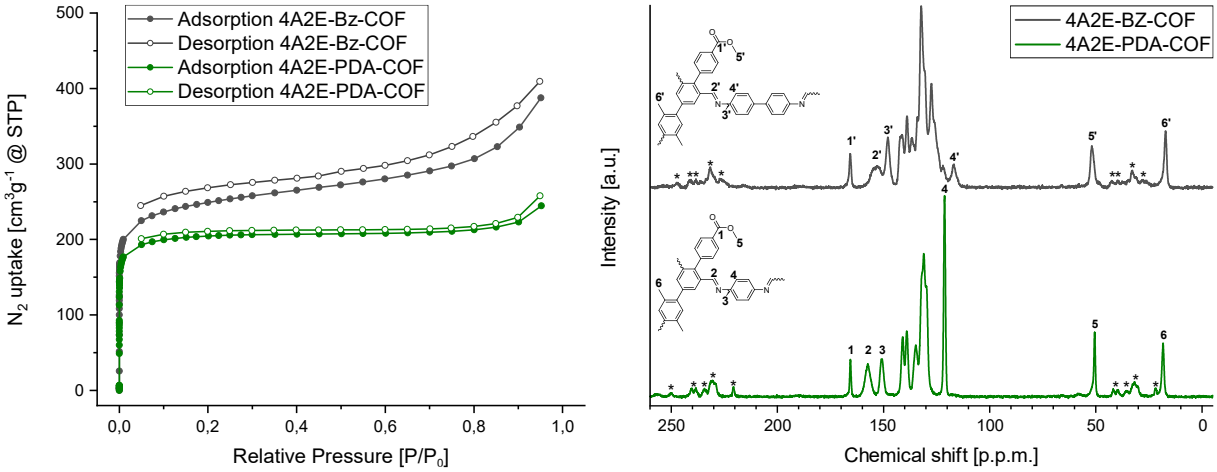

Figure 4: Nitrogen adsorption isotherms at 77 K (left) of **4A2E**-PDA- COF (green) and **4A2E**-Bz-COF (grey). ^{13}C-MAS NMR of **4A2E**-PDA-COF (grey) and **4A2E**-Bz-COF (green). Asterisks indicate spinning side bands.

It is known that the stacking can lead to symmetry reductions[25] or even complete changes of a PXRD pattern through the change in symmetry.[33] Therefore, we considered again the *kgm* structural model, and started building models with different stacking modes, to test if the stacking can explain the absence of the 100 peak in the PXRD and the TEM images. Slip stacking only leads to peak broadening or small peak splitting through apparent symmetry reduction,[25] but cannot explain the absence of one significant reflection. In AB stacking where one hexagonal pore stacks on top of a triangular pore, while one trigonal pore remains open, leads to a dramatic reduction, but not to a complete loss off intensity of the 100 peak in the simulated pattern. When simulating the ABC-stacking of the *kgm* net layers of the COF we obtained a good match with the simulated XRD pattern, which was also validated by Pawley refinement of the ABC-stacked structure. The ABC stacking leads to a change of the symmetry to $R\bar{3}$, the symmetry has a 3-fold screw axis, which leads to systematic absences in the X-Ray diffraction. The reflection conditions lead to a complete absence of the 100 reflection. Additionally, this structural model can explain the previously unexplained reflex at 7.85° 2θ (d=11.33 Å), which corresponds to the 101 reflection. The periodicity corresponding to the 101 reflections in the PXRD can also be observed in some crystal orientations in the TEM images (Figure 3 E, F). Explaining the presence of this reflection is important, as in typical hexagonal COFs with small parameters of c < 5 Å, no reflections are expected between the "first" and "second" reflection in a hexagonal unit cell, which normally correspond to the 100 and 110 reflections, respectively. In the $R\bar{3}$ space group of the ABC stacked **4A2E**-PDA-COF also requires the presence of three layers in one unit cell. While reflections such as 001 are not observed due to systematic absences (only *000l: l = 3n* are allowed), the 101 reflection is allowed as it fulfills the *hkil: −h+k+l = 3n* reflection condition. Therefore, the ABC stacked model of the **4A2E**-PDA-COF explains the absent and additional reflections in the PXRD fully, and matches well with the crystallites seen in cryo-TEM.

The ABC-stacking of the *kgm* layers leads to the "closing" of the larger triangular pores with the smaller hexagonal pores with small pore apertures of only around 7 Å, which leads to a pearl-string pore

structure, which is quite unusual for COFs (Figure S 4). The small pore apertures that are every third layer in the structure, imposed by the six phenyl methoxycarbonyl linkers protruding into the pore and nearly in contact with each other thereby dominate the adsorption properties and lead to only small micropores being observed in the structure. This highly crowded pore is exaggerated by the locking of the imine orientation away from the ortho- phenyl ring. This orientation was predicted by force field calculations and verified by the single crystal X-ray diffraction (SCXRD) structure of a model imine compound from aniline and a carboxy dialdehyde linker (Figure S 3). This orientation can be attributed to steric repulsion with the phenyl ring. Interestingly the interaction between the imine and the phenyl ring reduces the number of conformers[14] of the imine bond, which can be used to improve the crystallinity of COFs by forcing it to point away from the phenyl rings. Similar strategies can be realized with intramolecular hydrogen bonding[41] and ortho methoxy groups.[42]

To understand the preference for formation of the *kgm* structure over the *sql* structure in the **4A2E**-PDA-COF we used force field simulations to look at the interactions within one pore in unconstrained molecular models (Figure 5, A). In the hexagonal pore the methyl groups are in close contact but no out of plane bending is observed, which would be indicative of an overcrowded pore space. In the rhombic pore using also PDA, significant steric repulsion can be observed by the bulky functional groups bending out of each other's way (Figure 5, B). Interestingly, this situation is reinforced by the conformational locking of the imine groups, which forces the bulky functional groups closer to each other. We theorized that this close contact leads to repulsion and thereby disfavors the *sql* structure when using the short phenylene diamine linker. The close contact of the methyl groups across the pore in the *sql* net is directly related to the length of the diamine linker, where a longer diamine might relieve some of the steric repulsion. Simulation of a benzidine based rhombic pore (Figure 5, C) indeed showed less repulsion between the methyl groups despite close contact.

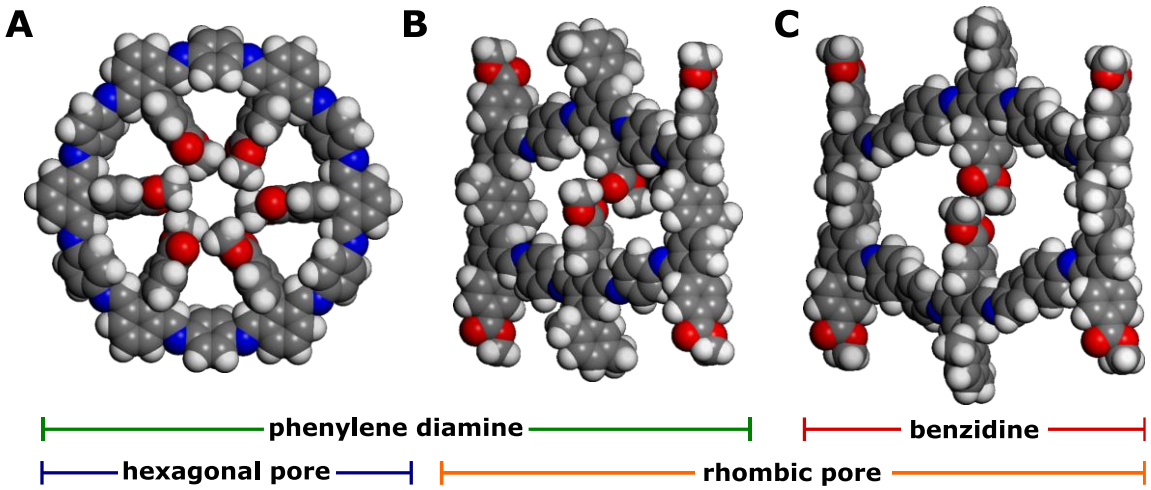

Figure 5: Unconstrained force field simulations of molecular analogs of one pore. A: Hexagonal pore with PDA as the amine. B: rhombic pore with PDA. C: Rhombic pore with benzidine.

To test this assumption experimentally, we synthesized the COF based on the tetraaldehyde and benzidine (Bz), which is significantly longer (N-N distance of 9.98 Å for Bz[43] vs. 5.66 Å for PDA[44], respectively), and therefore should lead to decreased repulsion between the ester groups. The benzidine based COF showed prominent reflexes in the PXRD at 4.60° and 6.44° with smaller broad and overlapping reflexes at 9.7°, 13.4°, 23.1° (Figure 2, E, F). This pattern can be modelled by a *sql* based structure with a primitive unit cell (Z=1). Lattice parameters and the local symmetry match well with the observed crystallites in the TEM (Figure 3 G, H). However, in the FFT additional periodicities can only be explained with a Z=2 superstructure, redefined with a = (110), b = (-110), c = (001) respective to the primitive unit cell. The additional periodicities of observed in the FFT then correspond

to the 410, 520 and 610 reflections. Supercell periodicities are observed in multiple crystallites in the TEM (Figure S 9, Figure S 10). We therefore modeled the structure of the **4A2E**-Bz-COF as a Z=2 unit cell in Materials Studio. Pawley refinement of the lattice parameters led to good agreement with the observed PXRD pattern (Figure 2, F), resulting in a unit cell with lattice parameters of: a = 27.5 Å, b =31.9 Å, c = 4.4 Å, α = 55.0°, β = 90°; γ = 86.6°. The deviation of γ from 90° dramatically improved the Pawley fit and matches with TEM images which showed γ = ~84°. The peak splitting at 6.44° indicated a symmetry reduction in the structure,[25] which was well explained with slip-stacking perpendicular to the **4A2E** linker in the structure. In *sql* lattice COFs, peak splitting can also be explained by a≠b structures,[45] however these refinements all led to chemical unreasonably small values of a and b during refinement. Additionally, the N_2-adsorption isotherm (Figure 4) match the expected structure well. The calculated BET surface was 774 m²/g.

The stoichiometric nature of 4A2E-Bz-COF was confirmed by IR spectroscopy and ssNMR (Figure S 7, Figure 4), where no significant aldehyde peak was detected at 190 ppm. Simultaneously, ssNMR revealed the characteristic peak of the quaternary carbon of the methyl ester (1') at 165 ppm, and the methyl ester carbon (5') could be assigned to the peak at 52 ppm for **4A2E**-Bz-COF (Figure S 11). The methyl ester peak is thus shifted downfield from the methyl group attached to the **4A2E** linker core, which is evident at 17 ppm.

Discussion

Force field calculations of the one pore model indicate that the formation of the hexagonal pore leads to a low steric demand of the bulky methyl benzoate functional groups, while in the rhombic pore the methyl benzoate groups are forced much closer to each other. This is especially prominent in the case of the short PDA linker. In the case of the longer benzidine, interaction of the methyl benzoate functional groups through the pore in the rhombic pore is still evident, but less pronounced than in the PDA case. This indicates that the steric interaction of the bulky functional groups, through the pore play a role in determining the formation of the net during the synthesis of the 4A2E-PDA-COF. It is difficult to predict, if the *sql* or *kgm* net are the "default" or more stable structure for a given linker, as weak interactions such as stacking play a role.[14] However, based on the same aldehyde linker, only with different length diamines we observed a switch in the preference from the *kgm* for the smaller diamine to the *sql* for the longer diamine. This indicates that the longer benzidine linker allows the formation of the *sql* structure while the shorter PDA linker prohibits the formation of the *sql* and thereby favors the formation of *kgm*. COF based on a similar tetra aldehyde linker as reported here, but without the bulky functional groups was reported to favor the formation of the *sql* COFs for both the benzidine and PDA linkers.[46] This supports the hypothesis, that the steric interactions drive the formation of the *kgm* lattice instead of the *sql*. We achieve a length dependent switch between the topologies for our COFs, which allows us to override those preferences via the weak interactions.

The formation of the ABC – stacking of the **4A2E**-PDA-COF is a rare example of this stacking type in the *kgm* net. Due to the dimethyl core and the methyl benzoate group in ortho position to the aldehyde groups, the **4A2E** linker possesses large dihedral angles along its backbone that inhibit efficient π-stacking of the linker in the resulting COF. This lack of strong interactions between the layers might be responsible for the formation of the ABC stacked structure. This feature of the linker might also be responsible for the slip stacking of the **4A2E**-Bz-COF, where the slip stacking relieves unfavorable close contact of the dimethyl benzene core of the linker. Another reason for the apparent rarity of the ABC-stacked *kgm* structures might be the misassignment of *sql* nets to ABC stacked *kgm* structures, as often the position of the reflection with the lowest angle in the PXRD is taken an indication of *kgm* vs. *sql*. The absence of the (100) reflection in $R\bar{3}$/ABC stacked *kgm* COFs leads to the first observed reflection (110) to be in approximately the same position as the (100) reflection of a *sql* lattice based on the same

linkers (in the case of the **4A2E**-Bz-COF it is the (110) reflection due to the super cell). In the COFs reported here, the differentiation between ABC-stacked *kgm* and *sql* is more straightforward, as the methyl benzoate leads to high intensity on reflections at larger angles, and only a very weak reflection at low angles in the *sql* case. This highlights the importance for TEM measurements to not only verify the *d*-spacings, but also the symmetries in the crystallites.

Conclusion

The toolbox for the COF geometry is mostly limited to the geometry of the linkers. For nets where polymorphism is possible, there is not yet a reliable synthesis, so that the outcome would be predictable. Sterically demanding moieties can change the geometry of the linker and thus influence which nets can be formed. This concept is utilized through the tuning of dihedral angle in COFs[47] and MOFs[48], where the ortho-substitution of linkers significantly impacts overall geometry. In our work, we influenced the net geometry through through-pore interactions, exploring weak interactions as a nuanced tool for fine-tuning. Through simulations of rhombic pores (Figure 5) that occur in the *sql* structures, we observed that smaller diamines lead to direct interactions between methyl benzoate moieties across the pore. The through-pore interactions are now of repulsive nature, but one might envision the design of attractive interactions that could reverse the trend observed here. By altering interactions not within a single linker but between neighboring linkers, it becomes conceivable to generate non-flat structures and transition the system into three-dimensional configurations. This work also shows that steric interactions need to be considered when designing highly functional COFs, as the side chains in COFs should not be neglected and can influence the structure significantly.

We successfully synthesized two new and exciting COFs, showcasing the versatility of COF design. For the convincing structural elucidation of **4A2E**-PDA-COF TEM data was necessary to provide good evidence for the ABC stacking. The synthesized linker, which has not previously been reported, offers the unique advantage of forming larger pores compared to COFs based on the reported [1,1′-biphenyl]-3,3′,5,5′-tetracarbaldehyde with a similar structural motif.[49] Those only form the *kgm* networks.

Acknowledgements

A.W. and F.H. gratefully acknowledge the Fonds der Chemischen Industrie (FCI) for their support through the Liebig Fellowship, and funding by the Deutsche Forschungsgemeinschaft (DFG, German Research foundation) through the RTG 2670 (project-ID 436494874). Further we acknowledge, Toni Kurt Traeger for support in the preparation of the TEM samples, Dr. Olaf Fuhr for data analysis of the SCXRD data and Jenny Bienias-Dragon for the sorption measurements. Dr. A. Krushelnitsky is thanked for conducting the solid-state NMR measurements. F.H. further acknowledges the YIG Prep Pro Fellowship that funded part of this project. This work was supported by the European Union through funding of the Horizon Europe ERA Chair “hot4cryo” project number 101086665 (to P.L.K.), by the Federal Ministry for Education and Research (BMBF, ZIK program) [Grant nos. 03Z22HI2, 03Z22HN23, and 03COV04 to P.L.K.], the European Regional Development Funds for Saxony-Anhalt [grant no. EFRE: ZS/2016/04/78115 to P.L.K.], funding by Deutsche Forschungsgemeinschaft (DFG) [project number 391498659, RTG 2467], and the Martin-Luther University of Halle-Wittenberg. This work was carried out with the support of the Karlsruhe Nano Micro Facility (KNMFi, www.knmf.kit.edu, Proposal Nr. 2022-028 031295), a Helmholtz Research Infrastructure at Karlsruhe Institute of Technology (KIT, www.kit.edu)

References

(1) Zhu, N.; Lennox, M. J.; Düren, T.; Schmitt, W. Polymorphism of Metal–Organic Frameworks: Direct Comparison of Structures and Theoretical N2-Uptake of Topological Pto- and Tbo-Isomers. *Chem. Commun.* **2014**, *50* (32), 4207–4210. https://doi.org/10.1039/C3CC49829H.

(2) Bon, V.; Senkovska, I.; Baburin, I. A.; Kaskel, S. Zr- and Hf-Based Metal–Organic Frameworks: Tracking Down the Polymorphism. *Cryst. Growth Des.* **2013**, *13* (3), 1231–1237. https://doi.org/10.1021/cg301691d.
(3) Liu, Y.; Li, J.; Lv, J.; Wang, Z.; Suo, J.; Ren, J.; Liu, J.; Liu, D.; Wang, Y.; Valtchev, V.; Qiu, S.; Zhang, D.; Fang, Q. Topological Isomerism in Three-Dimensional Covalent Organic Frameworks. *J. Am. Chem. Soc.* **2023**, *145* (17), 9679–9685. https://doi.org/10.1021/jacs.3c01070.
(4) Banerjee, T.; Haase, F.; Trenker, S.; Biswal, B. P.; Savasci, G.; Duppel, V.; Moudrakovski, I.; Ochsenfeld, C.; Lotsch, B. V. Sub-Stoichiometric 2D Covalent Organic Frameworks from Tri- and Tetratopic Linkers. *Nat. Commun.* **2019**, *10* (1), 2689. https://doi.org/10.1038/s41467-019-10574-6.
(5) Nguyen, H. L.; Gropp, C.; Yaghi, O. M. Reticulating 1D Ribbons into 2D Covalent Organic Frameworks by Imine and Imide Linkages. *J. Am. Chem. Soc.* **2020**, *142* (6), 2771–2776. https://doi.org/10.1021/jacs.9b13971.
(6) Zhang, B.; Mao, H.; Matheu, R.; Reimer, J. A.; Alshmimri, S. A.; Alshihri, S.; Yaghi, O. M. Reticular Synthesis of Multinary Covalent Organic Frameworks. *J. Am. Chem. Soc.* **2019**, *141* (29), 11420–11424. https://doi.org/10.1021/jacs.9b05626.
(7) Zhou, T.-Y.; Xu, S.-Q.; Wen, Q.; Pang, Z.-F.; Zhao, X. One-Step Construction of Two Different Kinds of Pores in a 2D Covalent Organic Framework. *J. Am. Chem. Soc.* **2014**, *136* (45), 15885–15888. https://doi.org/10.1021/ja5092936.
(8) Pang, Z.-F.; Xu, S.-Q.; Zhou, T.-Y.; Liang, R.-R.; Zhan, T.-G.; Zhao, X. Construction of Covalent Organic Frameworks Bearing Three Different Kinds of Pores through the Heterostructural Mixed Linker Strategy. *J. Am. Chem. Soc.* **2016**, *138* (14), 4710–4713. https://doi.org/10.1021/jacs.6b01244.
(9) Tu, J.; Song, W.; Chen, B.; Li, Y.; Chen, L. 2D Covalent Organic Frameworks with Kagome Lattice: Synthesis and Applications. *Chem. – Eur. J.* **2023**, *29* (66), e202302380. https://doi.org/10.1002/chem.202302380.
(10) Xing, G.; Zheng, W.; Gao, L.; Zhang, T.; Wu, X.; Fu, S.; Song, X.; Zhao, Z.; Osella, S.; Martínez-Abadía, M.; Wang, H. I.; Cai, J.; Mateo-Alonso, A.; Chen, L. Nonplanar Rhombus and Kagome 2D Covalent Organic Frameworks from Distorted Aromatics for Electrical Conduction. *J. Am. Chem. Soc.* **2022**, *144* (11), 5042–5050. https://doi.org/10.1021/jacs.1c13534.
(11) Peng, Y.; Li, L.; Zhu, C.; Chen, B.; Zhao, M.; Zhang, Z.; Lai, Z.; Zhang, X.; Tan, C.; Han, Y.; Zhu, Y.; Zhang, H. Intramolecular Hydrogen Bonding-Based Topology Regulation of Two-Dimensional Covalent Organic Frameworks. *J. Am. Chem. Soc.* **2020**, *142* (30), 13162–13169. https://doi.org/10.1021/jacs.0c05596.
(12) Dalapati, S.; Jin, E.; Addicoat, M.; Heine, T.; Jiang, D. Highly Emissive Covalent Organic Frameworks. *J. Am. Chem. Soc.* **2016**, *138* (18), 5797–5800. https://doi.org/10.1021/jacs.6b02700.
(13) Ascherl, L.; Sick, T.; Margraf, J. T.; Lapidus, S. H.; Calik, M.; Hettstedt, C.; Karaghiosoff, K.; Döblinger, M.; Clark, T.; Chapman, K. W.; Auras, F.; Bein, T. Molecular Docking Sites Designed for the Generation of Highly Crystalline Covalent Organic Frameworks. *Nat. Chem.* **2016**, *8* (4), 310–316. https://doi.org/10.1038/nchem.2444.
(14) Haase, F.; Lotsch, B. V. Solving the COF Trilemma: Towards Crystalline, Stable and Functional Covalent Organic Frameworks. *Chem. Soc. Rev.* **2020**, *49* (23), 8469–8500. https://doi.org/10.1039/D0CS01027H.
(15) Wu, Y.; Xu, H.; Chen, X.; Gao, J.; Jiang, D. A π-Electronic Covalent Organic Framework Catalyst: π-Walls as Catalytic Beds for Diels–Alder Reactions under Ambient Conditions. *Chem. Commun.* **2015**, *51* (50), 10096–10098. https://doi.org/10.1039/C5CC03457D.
(16) Leng, W.; Peng, Y.; Zhang, J.; Lu, H.; Feng, X.; Ge, R.; Dong, B.; Wang, B.; Hu, X.; Gao, Y. Sophisticated Design of Covalent Organic Frameworks with Controllable Bimetallic Docking for a Cascade Reaction. *Chem. – Eur. J.* **2016**, *22* (27), 9087–9091. https://doi.org/10.1002/chem.201601334.
(17) Rabbani, M. G.; Sekizkardes, A. K.; Kahveci, Z.; Reich, T. E.; Ding, R.; El-Kaderi, H. M. A 2D Mesoporous Imine-Linked Covalent Organic Framework for High Pressure Gas Storage Applications. *Chem. – Eur. J.* **2013**, *19* (10), 3324–3328. https://doi.org/10.1002/chem.201203753.
(18) Dalapati, S.; Jin, S.; Gao, J.; Xu, Y.; Nagai, A.; Jiang, D. An Azine-Linked Covalent Organic Framework. *J. Am. Chem. Soc.* **2013**, *135* (46), 17310–17313. https://doi.org/10.1021/ja4103293.

(19) Pang, Z.-F.; Zhou, T.-Y.; Liang, R.-R.; Qi, Q.-Y.; Zhao, X. Regulating the Topology of 2D Covalent Organic Frameworks by the Rational Introduction of Substituents. *Chem. Sci.* **2017**, *8* (5), 3866–3870. https://doi.org/10.1039/C6SC05673C.
(20) Shi, X.; Yi, L.; Deng, H. Covalent Organic Frameworks Catalyzed by Organic Lewis Acid. *Sci. China Chem.* **2022**, *65* (7), 1315–1320. https://doi.org/10.1007/s11426-022-1272-5.
(21) Liang, R.-R.; Cui, F.-Z.; A, R.-H.; Qi, Q.-Y.; Zhao, X. A Study on Constitutional Isomerism in Covalent Organic Frameworks: Controllable Synthesis, Transformation, and Distinct Difference in Properties. *CCS Chem.* **2020**, *2* (2), 139–145. https://doi.org/10.31635/ccschem.020.201900094.
(22) Yu, X.-K.; Zhao, H.-Y.; Li, J.-P.; Li, X.-J.; Yang, J.-Q.; Zhu, Y.-L.; Lu, Z. Mechanism for Topology Selection of Isomeric Two-Dimensional Covalent Organic Frameworks. *J. Phys. Chem. Lett.* **2022**, *13* (30), 7087–7093. https://doi.org/10.1021/acs.jpclett.2c01743.
(23) Zhang, Y.; Položij, M.; Heine, T. Statistical Representation of Stacking Disorder in Layered Covalent Organic Frameworks. *Chem. Mater.* **2022**, *34* (5), 2376–2381. https://doi.org/10.1021/acs.chemmater.1c04365.
(24) Pütz, A.; Terban, M.; Bette, S.; Haase, F.; Dinnebier, R.; Lotsch, B. V. Total Scattering Reveals the Hidden Stacking Disorder in a 2D Covalent Organic Framework. *Chem. Sci.* **2020**, *11*, 12647–12654. https://doi.org/10.1039/D0SC03048A.
(25) Haase, F.; Gottschling, K.; Stegbauer, L.; Germann, L. S.; Gutzler, R.; Duppel, V.; Vyas, V. S.; Kern, K.; Dinnebier, R. E.; Lotsch, B. V. Tuning the Stacking Behaviour of a 2D Covalent Organic Framework through Non-Covalent Interactions. *Mater. Chem. Front.* **2017**, *1* (7), 1354–1361. https://doi.org/10.1039/C6QM00378H.
(26) Rawat, K. S.; Borgmans, S.; Braeckevelt, T.; Stevens, C. V.; Van Der Voort, P.; Van Speybroeck, V. How the Layer Alignment in Two-Dimensional Nanoporous Covalent Organic Frameworks Impacts Its Electronic Properties. *ACS Appl. Nano Mater.* **2022**, *5* (10), 14377–14387. https://doi.org/10.1021/acsanm.2c02647.
(27) Pelkowski, C. E.; Natraj, A.; Malliakas, C. D.; Burke, D. W.; Bardot, M. I.; Wang, Z.; Li, H.; Dichtel, W. R. Tuning Crystallinity and Stacking of Two-Dimensional Covalent Organic Frameworks through Side-Chain Interactions. *J. Am. Chem. Soc.* **2023**, *145* (40), 21798–21806. https://doi.org/10.1021/jacs.3c03868.
(28) Wang, H.; Yang, C.; Chen, F.; Zheng, G.; Han, Q. A Crystalline Partially Fluorinated Triazine Covalent Organic Framework for Efficient Photosynthesis of Hydrogen Peroxide. *Angew. Chem. Int. Ed.* **2022**, *61* (19), e202202328. https://doi.org/10.1002/anie.202202328.
(29) Alahakoon, S. B.; McCandless, G. T.; Karunathilake, A. A. K.; Thompson, C. M.; Smaldone, R. A. Enhanced Structural Organization in Covalent Organic Frameworks Through Fluorination. *Chem. – Eur. J.* **2017**, *23* (18), 4255–4259. https://doi.org/10.1002/chem.201700412.
(30) Alahakoon, S. B.; Tan, K.; Pandey, H.; Diwakara, S. D.; McCandless, G. T.; Grinffiel, D. I.; Durand-Silva, A.; Thonhauser, T.; Smaldone, R. A. 2D-Covalent Organic Frameworks with Interlayer Hydrogen Bonding Oriented through Designed Nonplanarity. *J. Am. Chem. Soc.* **2020**, *142* (30), 12987–12994. https://doi.org/10.1021/jacs.0c03409.
(31) Smirnova, O.; Ojha, S.; De, A.; Schneemann, A.; Haase, F.; Knebel, A. Tiny Windows in Reticular Nanomaterials for Molecular Sieving Gas Separation Membranes. *Adv. Funct. Mater.* **2023**, 2306202. https://doi.org/10.1002/adfm.202306202.
(32) Wu, X.; Han, X.; Liu, Y.; Liu, Y.; Cui, Y. Control Interlayer Stacking and Chemical Stability of Two-Dimensional Covalent Organic Frameworks via Steric Tuning. *J. Am. Chem. Soc.* **2018**, *140* (47), 16124–16133. https://doi.org/10.1021/jacs.8b08452.
(33) Wang, Z.; Zhang, Y.; Wang, T.; Lin, E.; Wang, T.; Chen, Y.; Cheng, P.; Zhang, Z. Modulating the Interlayer Stacking of Covalent Organic Frameworks for Efficient Acetylene Separation. *Small* **2023**, *19* (32), 2303684. https://doi.org/10.1002/smll.202303684.
(34) Yang, S.; Li, X.; Qin, Y.; Cheng, Y.; Fan, W.; Lang, X.; Zheng, L.; Cao, Q. Modulating the Stacking Model of Covalent Organic Framework Isomers with Different Generation Efficiencies of Reactive Oxygen Species. *ACS Appl. Mater. Interfaces* **2021**, *13* (25), 29471–29481. https://doi.org/10.1021/acsami.1c03170.

(35) Li, L.; Yun, Q.; Zhu, C.; Sheng, G.; Guo, J.; Chen, B.; Zhao, M.; Zhang, Z.; Lai, Z.; Zhang, X.; Peng, Y.; Zhu, Y.; Zhang, H. Isoreticular Series of Two-Dimensional Covalent Organic Frameworks with the Kgd Topology and Controllable Micropores. *J. Am. Chem. Soc.* **2022**, *144* (14), 6475–6482. https://doi.org/10.1021/jacs.2c01199.
(36) Huang, C.; Zhou, S.; Chen, C.; Wang, X.; Ding, R.; Xu, Y.; Cheng, Z.; Ye, Z.; Sun, L.; Wang, Z.; Hu, D.; Jia, X.; Zhang, G.; Gao, S. Biodegradable Redox-Responsive AIEgen-Based-Covalent Organic Framework Nanocarriers for Long-Term Treatment of Myocardial Ischemia/Reperfusion Injury. *Small* **2022**, *18* (47), 2205062. https://doi.org/10.1002/smll.202205062.
(37) Gao, Q.; Li, X.; Ning, G.-H.; Xu, H.-S.; Liu, C.; Tian, B.; Tang, W.; Loh, K. P. Covalent Organic Framework with Frustrated Bonding Network for Enhanced Carbon Dioxide Storage. *Chem. Mater.* **2018**, *30* (5), 1762–1768. https://doi.org/10.1021/acs.chemmater.8b00117.
(38) Vijayakumar, S.; Ajayaghosh, A.; Shankar, S. Expanding the Horizons of Covalent Organic Frameworks: Sub-Stoichiometric Synthesis as an Emerging Toolkit for Functional COFs. *J. Mater. Chem. A* **2023**. https://doi.org/10.1039/D3TA05715A.
(39) Haase, F.; Troschke, E.; Savasci, G.; Banerjee, T.; Duppel, V.; Dörfler, S.; Grundei, M. M. J.; Burow, A. M.; Ochsenfeld, C.; Kaskel, S.; Lotsch, B. V. Topochemical Conversion of an Imine- into a Thiazole-Linked Covalent Organic Framework Enabling Real Structure Analysis. *Nat. Commun.* **2018**, *9* (1), 2600. https://doi.org/10.1038/s41467-018-04979-y.
(40) De Bolòs, E.; Martínez-Abadía, M.; Hernández-Culebras, F.; Haymaker, A.; Swain, K.; Strutyński, K.; Weare, B. L.; Castells-Gil, J.; Padial, N. M.; Martí-Gastaldo, C.; Khlobystov, A. N.; Saeki, A.; Melle-Franco, M.; Nannenga, B. L.; Mateo-Alonso, A. A Crystalline 1D Dynamic Covalent Polymer. *J. Am. Chem. Soc.* **2022**, *144* (34), 15443–15450. https://doi.org/10.1021/jacs.2c06446.
(41) Chen, X.; Huang, N.; Gao, J.; Xu, H.; Xu, F.; Jiang, D. Towards Covalent Organic Frameworks with Predesignable and Aligned Open Docking Sites. *Chem. Commun.* **2014**, *50* (46), 6161–6163. https://doi.org/10.1039/C4CC01825G.
(42) Lyle, S. J.; Osborn Popp, T. M.; Waller, P. J.; Pei, X.; Reimer, J. A.; Yaghi, O. M. Multistep Solid-State Organic Synthesis of Carbamate-Linked Covalent Organic Frameworks. *J. Am. Chem. Soc.* **2019**, *141* (28), 11253–11258. https://doi.org/10.1021/jacs.9b04731.
(43) Rafilovich, M.; Bernstein, J. CCDC 625721: Experimental Crystal Structure Determination, 2007. https://doi.org/10.5517/CCP03KB.
(44) Ichikawa, Y.; Hiramatsu, M.; Mita, Y.; Makishima, M.; Matsumoto, Y.; Masumoto, Y.; Muranaka, A.; Uchiyama, M.; Hashimoto, Y.; Ishikawa, M. *Meta* -Non-Flat Substituents: A Novel Molecular Design to Improve Aqueous Solubility in Small Molecule Drug Discovery. *Org. Biomol. Chem.* **2021**, *19* (2), 446–456. https://doi.org/10.1039/D0OB02083D.
(45) Lin, S.; Diercks, C. S.; Zhang, Y.-B.; Kornienko, N.; Nichols, E. M.; Zhao, Y.; Paris, A. R.; Kim, D.; Yang, P.; Yaghi, O. M.; Chang, C. J. Covalent Organic Frameworks Comprising Cobalt Porphyrins for Catalytic CO2 Reduction in Water. *Science* **2015**, *349* (6253), 1208–1213. https://doi.org/10.1126/science.aac8343.
(46) Cao, X.; Jin, Y.; Wang, H.; Ding, X.; Liu, X.; Yu, B.; Zhan, X.; Jiang, J. A Tetraaldehyde-Derived Porous Organic Cage and Covalent Organic Frameworks. Syntheses, Structures, and Iodine Vapor Capture. *Chin. Chem. Lett.* **2023**, 109201. https://doi.org/10.1016/j.cclet.2023.109201.
(47) Gao, C.; Li, J.; Yin, S.; Sun, J.; Wang, C. Twist Building Blocks from Planar to Tetrahedral for the Synthesis of Covalent Organic Frameworks. *J. Am. Chem. Soc.* **2020**, *142* (8), 3718–3723. https://doi.org/10.1021/jacs.9b13824.
(48) Eddaoudi, M.; Kim, J.; O'Keeffe, M.; Yaghi, O. M. Cu2[o-Br-C6H3(CO2)2]2(H2O)2·(DMF)8(H2O)2: A Framework Deliberately Designed To Have the NbO Structure Type. *J. Am. Chem. Soc.* **2002**, *124* (3), 376–377. https://doi.org/10.1021/ja017154e.
(49) Tian, Y.; Xu, S.-Q.; Liang, R.-R.; Qian, C.; Jiang, G.-F.; Zhao, X. Construction of Two Heteropore Covalent Organic Frameworks with Kagome Lattices. *CrystEngComm* **2017**, *19* (33), 4877–4881. https://doi.org/10.1039/C7CE00590C.
(50) Drewry, J. A.; Duodu, E.; Mazouchi, A.; Spagnuolo, P.; Burger, S.; Gradinaru, C. C.; Ayers, P.; Schimmer, A. D.; Gunning, P. T. Phosphopeptide Selective Coordination Complexes as Promising

Src Homology 2 Domain Mimetics. *Inorg. Chem.* **2012**, *51* (15), 8284–8291. https://doi.org/10.1021/ic3008393.
(51) Grosjean, S.; Hassan, Z.; Wöll, C.; Bräse, S. Diverse Multi-Functionalized Oligoarenes and Heteroarenes for Porous Crystalline Materials. *Eur. J. Org. Chem.* **2019**, *2019* (7), 1446–1460. https://doi.org/10.1002/ejoc.201801232.
(52) Dolomanov, O. V.; Bourhis, L. J.; Gildea, R. J.; Howard, J. a. K.; Puschmann, H. OLEX2: A Complete Structure Solution, Refinement and Analysis Program. *J. Appl. Crystallogr.* **2009**, *42* (2), 339–341. https://doi.org/10.1107/S0021889808042726.
(53) Sheldrick, G. M. SHELXT – Integrated Space-Group and Crystal-Structure Determination. *Acta Crystallogr. Sect. Found. Adv.* **2015**, *71* (1), 3–8. https://doi.org/10.1107/S2053273314026370.
(54) Sheldrick, G. M. Crystal Structure Refinement with SHELXL. *Acta Crystallogr. Sect. C Struct. Chem.* **2015**, *71* (1), 3–8. https://doi.org/10.1107/S2053229614024218.

Supplementary information for

Enhancing Structural Control in Covalent Organic Frameworks through Steric Interaction-Driven Linker Design

Alena Winter, Farzad Hamdi, Andreas Eichhöfer, Kay Saalwächter, Panagiotis Kastritis, Frederik Haase*

Linker Synthesis

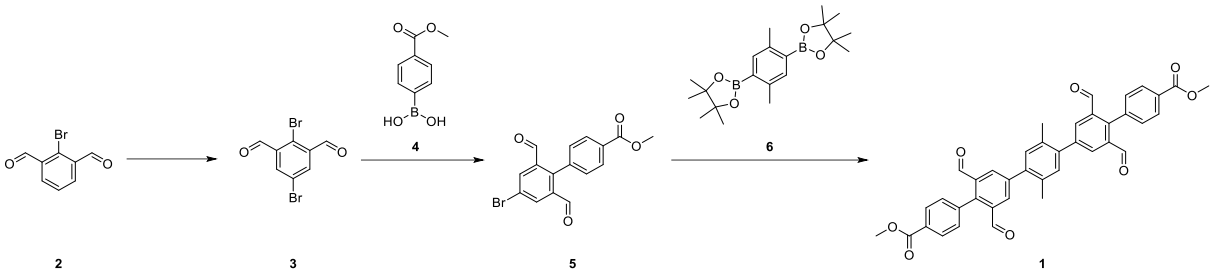

Figure S 1: Synthesis strategy of the **4A2E** linker.

2,5-Dibromoisophthalaldehyde (3)[50]

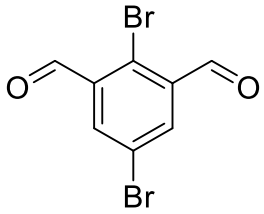

In a 50 mL crimp vial, 2-bromoisophthalaldehyde (5.00 g, 23.5 mmol, 1.00 equiv.) and *N*-bromosuccinimide (5.00 g, 28.1 mmol, 1.20 equiv.) was dissolved in concentrated sulfuric acid (25 mL) and stirred at 85 °C for 16 h. The solution was poured into a solution of a stoichiometric amount of sodium bicarbonate in water and the product was extracted several times into dichloromethane (DCM). The solvent was removed under reduced pressure and the residue was purified by flash chromatography (CH/DCM; 1:1). The product was obtained as an off-white solid in a yield of 69% (4.76 g).

^{1}H NMR (400 MHz, $CDCl_3$) δ [ppm] = 10.46 (s, 2 H), 8.22 (s, 2 H)

^{13}C NMR (100 MHz, $CDCl_3$) δ [ppm] = 189.31, 137.80, 135.83, 128.76, 123.24

Methyl 4'-bromo-2',6'-diformyl-[1,1'-biphenyl]-4-carboxylate (4)

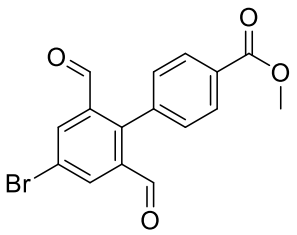

In a 100 mL 3-neck flask, 2,5-dibromoisophthalaldehyde (1.00 g, 3.42 mmol, 1.25 equiv.) and (4-methoxycarbonylphenyl)boronic acid (493 mg, 2.74 mmol, 1.00 equiv.) were dissolved in dry 1,4-dioxane (15 mL) and bubbled for 20 min. Pd(dppf)Cl_2 (100 mg, 137 µmol, 5 mol%) was added and the solution was bubbled for additional 10 min. K_3PO_4 (1.74 g, 8.22 mmol, 3.00 equiv.) was dissolved in water (5 mL) and degassed for 10 min. Afterwards it was added to the reaction mixture. The reaction was stirred at 90 °C for 16 h. After cooling to room temperature, the reaction mixture was filtered and the solvents were removed under reduced pressure. The precipitate was dissolved in DCM (40 mL) and washed with water (3 * 50 mL) and brine (1 * 50 mL). The organic phase was dried over Na_2SO_4 and evaporated under reduced pressure. The crude residue was purified via flash column chromatography (CH:EtOAc). A higher catalyst concentration leads to dehalogenation reaction. Yield: 599 mg (63%, 1.73 mmol)

^{1}H NMR (400 MHz, $CDCl_3$) δ [ppm] = 9.71 (s, 2 H), 8.36 (s, 2 H), 8.21 (d, J = 8.5 Hz, 2 H), 7.47 (d, J = 8.5 Hz, 2 H), 3.99 (s, 3 H)

^{13}C NMR (100 MHz, $CDCl_3$) δ [ppm] = 188.9, 166.3, 145.2, 136.5, 136.2, 135.6, 131.4, 130.9, 130.0, 124.0, 52.7

The substitution pattern was also verified via X-ray structure analysis of a single crystal grown by slow evaporation of $CDCl_3$. The crystal structure has been deposited to the CCDC under the number: CCDC-2312146.

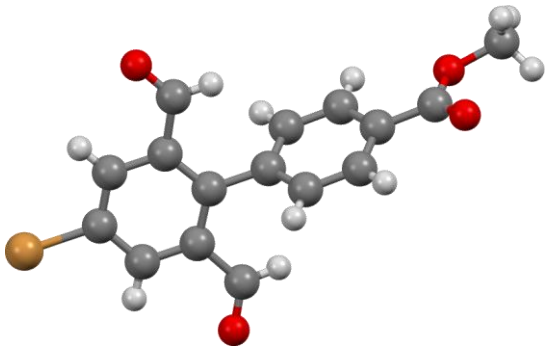

Figure S 2: 3D structure of Methyl 4'-bromo-2',6'-diformyl-[1,1'-biphenyl]-4-carboxylate confirming the cross coupling at the 1' position.

1,4-Bis(pinacolatoboronyl)-2,5-dimethylbenzene (6)

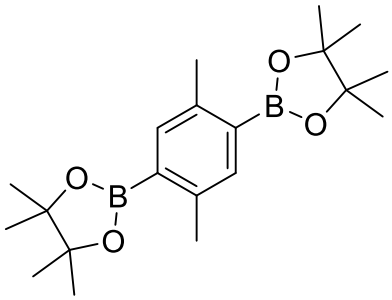

Following a literature procedure[51], in a 50 mL crimp vial under a nitrogen atmosphere, 2,5-dibromo-*p*-xylene (1.06 g, 4.00 mmol, 1.00 equiv.), B_2pin_2 (3.05 g, 12.0 mmol, 3.00 equiv.), $Pd(dppf)Cl_2$ (0.196 g, 0.24 mmol, 0.06 equiv.), and KOAc (2.36 g, 24.0 mmol, 6.00 equiv.) were dissolved in dry DMF(40 mL) and degassed with N_2 for 20 min. The reaction mixture was heated at 85 °C for 48 h. The reaction mixture was cooled down to room temperature, then added to water before being extracted with DCM (50 mL). Combined organic layers were washed with water (2 * 100 mL) and brine (100 mL), then dried with Na2SO4 and evaporated under reduced pressure. The crude product was purified by recrystallization in MeOH. The product was obtained as a beige solid in a yield of 77% (1.11 g)

^{1}H NMR (400 MHz, $CDCl_3$) δ [ppm] = 7.53 (s, 2 H), 2.48 (s, 6 H), 1.34 (s, 24 H)

^{13}C NMR (100 MHz, $CDCl_3$) δ [ppm] = 140.69, 137.05, 83.55, 25.03, 21.62

Dimethyl 2',3''',5''',6'-tetraformyl-2'',5''-dimethyl-[1,1':4',1'':4'',1''':4''',1'''':4'''',1''''-quinquephenyl]-4,4''''-dicarboxylate (4A2E)

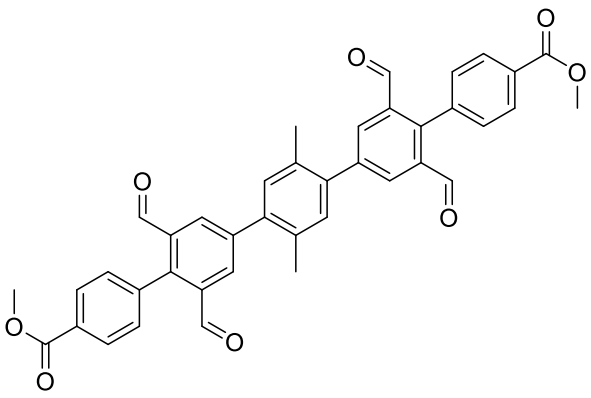

In a 100 mL 3-neck flask under a nitrogen atmosphere, methyl 4'-bromo-2',6'-diformyl-[1,1'-biphenyl]-4-carboxylate (882 mg, 2.54 mmol, 2.50 equiv:), 1,4-Bis(pinacolatoboronyl)-2,5-dimethylbenzene (362 mg, 1.01 mmol, 1.00 equiv:) and $Pd(PPh_3)_4$ (133 mg, 115 µmol, 0.10 equiv) were dissolved in a mixture of dry toluene and dry 1,4-dioxane (1:1; 16 mL) and degassed with N_2 for 15 min. K_2CO_3 (796 mg, 5.76 mmol, 5.00 equiv.), dissolved in water (4 mL), was degassed for 10 min and added to the reaction mixture. The reaction was heated to 110 °C for 16 h. After the reaction cooled down to room temperature, the insoluble precipitate was filtered off and washed with EtOAc and water and dissolved in DCM (White solid). To increase the yield, the organic phase of the reaction mixture was washed with water (2 * 20 mL). After phase separation, the aqueous phase was extracted with DCM (3* 20 mL). The combined organic extracts were dried over Na_2SO_4 and the solvent was removed under reduced pressure. The crude material was purified *via* column chromatography of silica gel with CH/DCM as an eluent.

Yield: 477 mg (74%, 0.747 mmol)

^{1}H NMR (400 MHz, $CDCl_3$) δ [ppm] = 9.86 (s, 4 H), 8.30 (s, 4 H), 8.25 (d, J = 8.5 Hz, 4 H), 7.56 (d, J = 8.5 Hz, 4 H), 7.27 (s, 2 H), 4.01 (s, 6 H), 2.36 (s, 6 H)

^{13}C NMR (100 MHz, $CDCl_3$) δ [ppm] = 190.19, 166.25, 145.23, 142.36, 139.07, 137.29, 134.61, 133.28, 133.15, 132.14,130.99, 130.95, 129.74, 42.48, 19.84

Model compound synthesis

Methyl 2',6'-diformyl-[1,1'-biphenyl]-4-carboxylate

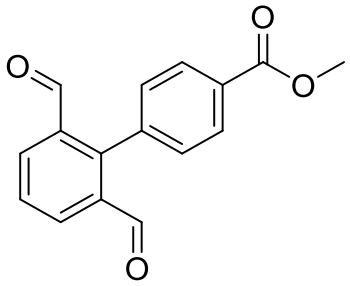

Under nitrogen atmosphere in a 50 mL crimp vial, 2-bromobenzene-1,3-dicarbaldehyde (2.43 g, 11.4 mmol, 1.00 equiv), (4-methoxycarbonylphenyl)boronic acid (3.08 g, 17.1 mmol, 1.50 equiv), potassium carbonate (4.73 g, 34.2 mmol, 3.00 equiv) and dichloropalladium;triphenylphosphane (401 mg, 571 µmol, 0.0500 equiv) were dissolved in dry 1,4-dioxane (20.0 mL) and degassed for 10 min. Degassed water (5.00 mL) was added and the reaction was heated to 100 °C for 4 h. The reaction mixture was cooled down, diluted with DCM and washed with water and brine. Difficulties in the phase separation. The organic phase was dried over $MgSO_4$. The crude residue was was purified via flash column chromatography (30% DCM in CH to 100% DCM). Yield: 1.35 g (44%, 5.02 mmol)

^{1}H NMR (400 MHz, $CDCl_3$) δ [ppm] = 9.78 (s, 2 H), 8.27 (d, J = 7.7 Hz, 2 H), 8.21 (d, J = 8.2 Hz, 2 H), 7.71 (t, J = 7.7 Hz , 1H) 7.48 (d, J = 8.2 Hz, 2 H), 3.99 (s, 3 H)

^{13}C NMR (100 MHz, $CDCl_3$) δ [ppm] = 188.8, 166.2, 145.1, 136.4, 136.1, 135.5, 131.3, 130.9, 129.9, 123.9, 52.6

Methyl 2’,6’-bis[(phenylimino)methyl][1,1’-biphenyl]-4-carboxylate

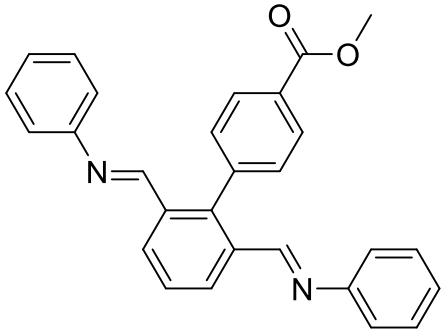

Methyl 2',6'-diformyl-[1,1'-biphenyl]-4-carboxylate (25.0 mg, 93.2 µmol, 1.00 equiv) and aniline (17.0 µL, 17.4 mg, 186 µmol, 2.00 equiv) were dissolved in deuterated chloroform (500 µL). The reaction mixture was stirred at 60 °C for 4 h. Crystals were grown by slow evaporation of CDCl3. The structure was verified by single crystal X-ray analysis and has been deposited to the CCDC under the number: CCDC- 2312147.

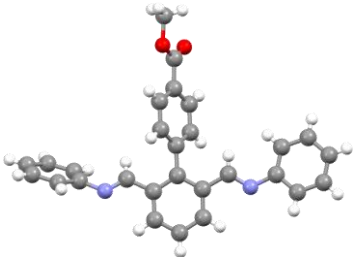

Figure S 3: 3D structure of Methyl 2’,6’-bis[(phenylimino)methyl][1,1’-biphenyl]-4-carboxylate showing the imine-nitrogen pointing away from the ortho phenyl ring.

COF synthesis

4A2E-PDA-COF: A 50 mL vial was charged with tetraaldehyde linker (59.4 mg, 0.093 mmol, 1.00 equiv.). It was suspended in a mixture 1,4-dioxane/mesitylene (550 µL:4.4 mL). TFA (114.6 µL, 170.6 mg, 1.50 mmol, 16.0 equiv.) was added and subsequently phenylenediamine (20.19 mg, 1.87 mmol, 2.00 equiv., dissolved in 550 µL 1,4-dioxane) was added. The vial was closed and placed in the ultrasonic bath for 10 min. The mixture was heated in an oven at 120 °C for 3 days. After being cooled to room temperature, the solvent was filtered of and the solid was washed thoroughly with methanol. Soxhlet extraction with MeOH overnight followed by supercritical CO_2 drying yielded PDA-COF as a yellow solid.

4A2E-Bz-COF: A 50 mL vial was charged with tetraaldehyde linker (59.75 mg, 0.0935 mmol, 1.00 equiv.). It was suspended in a mixture 1,4-dioxane/mesitylene (1.1 mL:4.4 mL). TFA (453.2 µL, 674.81 mg, 5.92 mmol, 63.3 equiv.) was added and subsequently benzidine (34.45 mg, 1.87 mmol, 2.00 equiv.) was added. The vial was closed and placed in the ultrasonic bath for 10 min. The mixture was heated in an oven at 120 °C for 3 days. After being cooled to room temperature, the solvent was filtered of and the solid was washed thoroughly with methanol. Soxhlet extraction with MeOH overnight followed by supercritical CO_2 drying yielded BZ-COF as a yellow solid.

Methods

Materials and methods

All materials were obtained from commercial sources (TCI, BLD Pharm, abcr, Sigma Aldrich, FisherScientific/ThermoFisher)

NMR: The solution state NMR spectra were acquired using an Agilent Technologies 400 MHz VNMRS and 500 MHz DD2 spectrometer at a temperature of 27 °C. The chemical shifts (denoted as δ) are presented in parts per million (ppm) and are calibrated with respect to the residual signal of the solvent ($CDCl_3$: 7.26 ppm for ^1H and 77.16 ppm for ^{13}C)

ssNMR: The ^{13}C CP-MAS spectra were obtained on a Bruker Avance III spectrometer with proton resonance frequency 400 MHz. The samples were packed in 4 mm rotors and spun at MAS rate 10 kHz at ambient temperature. Experimental parameters: CP contact time 2.5 ms, ^1H 90-degree pulse 3.6 microseconds; the ^{13}C signal was recorded during 35 ms with 65 kHz SPINAL proton decoupling.

IR: Measurements were conducted using a DiaMaxATR unit (Harrik, Pleasantville, NY, USA), which was integrated with a Tensor 27 spectrometer (BRUKER, Billerica, USA). The sample was applied onto the ATR crystal and compressed using the pressure applicator, featuring a force-limited slip-clutch mechanism. The experiment was carried out at room temperature and consisted of 256 accumulations, with data acquisition managed by the OPUS software. Subsequently, background-corrected spectra were analyzed using the OPUS software and further processed in Origin.

N_2-sorption: All N_2-sorption measurements were carried out using a Quantachrome autosorb iQ2. Before gas adsorption measurements, the sample was activated by drying under a vacuum at 120 °C for 16 h. The resulting sample was then used for gas adsorption measurements from 0 to 1 atm at 77 K. The Brunauer-Emmett-Teller (BET) method was utilized to calculate the specific surface areas. By using the non-local density function theory model, the pore size distribution curves were derived from the sorption data.

PXRD: Measurements were conducted with an Incoatec (Geesthacht, Germany) IμS equipped with a microfocus source and a monochromator for CuKα radiation (l=1.54 Å). The 2D scattering patterns were captured using a Vantec 500 2D detector (Bruker AXS, Karlsruhe).

TEM: The COF sample was suspended in 1-butanol at a concentration of 2 mg/mL. This suspension underwent an 8-minute sonication process at room temperature in a standard ultrasonic bath (Bandelin Sonorex Digiplus - Bandelin Electronic GmbH & Co. KG) and was subsequently centrifuged at 17,000 g for 3 minutes (Heraeus Fresco 21 - ThermoFisher Scientific). Following this, a 3.5 µl aliquot of the supernatant 1-butanol was dispensed onto the carbon side of lacey grids, which were already laid on 525-type ashless filter paper to remove excess solution. This technique enables the lacey film to selectively filter fine COF particles. Subsequently, the grids were air-dried and then securely affixed within the ThermoFisher Autogrid assembly using the standard tools, all conducted at room temperature.

The prepared samples were loaded into a Thermo Fisher Scientific Glacios cryogenic electron microscope, operating at 200 kV and equipped with a Falcon 4i direct electron detector. These samples were left to equilibrate overnight under vacuum conditions within the microscope's autoloader at room temperature to ensure thorough drying. Following this, the samples were gradually cooled to cryogenic temperatures (below 100 °K) inside the microscope while maintaining the vacuum.

For imaging, a low-dose strategy was employed. Images were captured with an average electron dose of 50 e/Å² at a pixel size of 0.936 Å in electron counting mode, and a frame rate of 310/s. The electron

event data underwent motion correction and were stored as a single frame using the on-the-fly frame alignment feature of the Falcon 4i camera.

Single Crystal X-ray Analysis: Diffraction data of Methyl 4'-bromo-2',6'-diformyl-[1,1'-biphenyl]-4-carboxylate (**4**) and Methyl 2',6'-bis[(phenylimino)methyl][1,1'-biphenyl]-4-carboxylate were collected on a STOE STADI VARI diffractometer with monochromated Mo Kα (0.71073 Å) or Ga Kα (1.34143 Å) radiation at low temperature. Using Olex2[52], the structures were solved with the ShelXT[53] structure solution program using Intrinsic Phasing and refined with the ShelXL[54] refinement package using Least Squares minimization. Refinement was performed with anisotropic temperature factors for all non-hydrogen atoms; hydrogen atoms were calculated on idealized positions. Crystallographic data and refinement details are summarized in Table S1.

Table S1 Crystallographic data and refinement details.

Compound	Methyl 4'-bromo-2',6'-diformyl-[1,1'-biphenyl]-4-carboxylate (**4**)	Methyl 2',6'-bis[(phenylimino)methyl][1,1'-biphenyl]-4-carboxylate
Empirical formula	$C_{16}H_{11}BrO_4$	$C_{28}H_{22}N_2O_2$
Formula weight	347.16	418.47
Temperature/K	180.0	180
Crystal system	orthorhombic	triclinic
Space group	$Pna2_1$	$P\bar{1}$
a/Å	14.3243(10)	9.9945(16)
b/Å	11.4688(7)	10.1084(12)
c/Å	8.7762(8)	11.4916(15)
α/°	90	82.539(10)
β/°	90	73.454(11)
γ/°	90	76.360(11)
Volume/Å^3	1441.78(19)	1079.1(3)
Z	4	2
ρ_{calc}g/cm^3	1.599	1.288
μ/mm^{-1}	2.757	0.082
F(000)	696.0	440.0
Crystal size/mm^3	0.08 × 0.058 × 0.015	0.22 × 0.2 × 0.18
Radiation	Ga Kα (λ = 1.34143)	Mo Kα (λ = 0.71073)
2Θ range for data collection/°	12.29–128.0	3.71–52.0
Index ranges	–18 ≤ h ≤ 17, –15 ≤ k ≤ 11, –11 ≤ l ≤ 9	–12 ≤ h ≤ 12, –12 ≤ k ≤ 9, –14 ≤ l ≤ 14
Reflections collected	9338	8450
Independent reflections	2842 [R_{int} = 0.0630]	4194 [R_{int} = 0.1187]
Ind. refl. with I≥2σ (I)	2277	2078
Data/restraints/parameters	2842/1/191	4194/0/290
Goodness-of-fit on F^2	1.031	0.973
Final R indexes [I≥2σ (I)]	R_1 = 0.0383, wR_2 = 0.0973	R_1 = 0.1171, wR_2 = 0.2769
Final R indexes [all data]	R_1 = 0.0485, wR_2 = 0.1020	R_1 = 0.1826, wR_2 = 0.3287
Largest diff. peak/hole / e Å^{-3}	0.40/–0.52	0.55/–0.73
Flack parameter	–0.05(3)	
CCDC number	2312146	2312147

Supplemental Figures

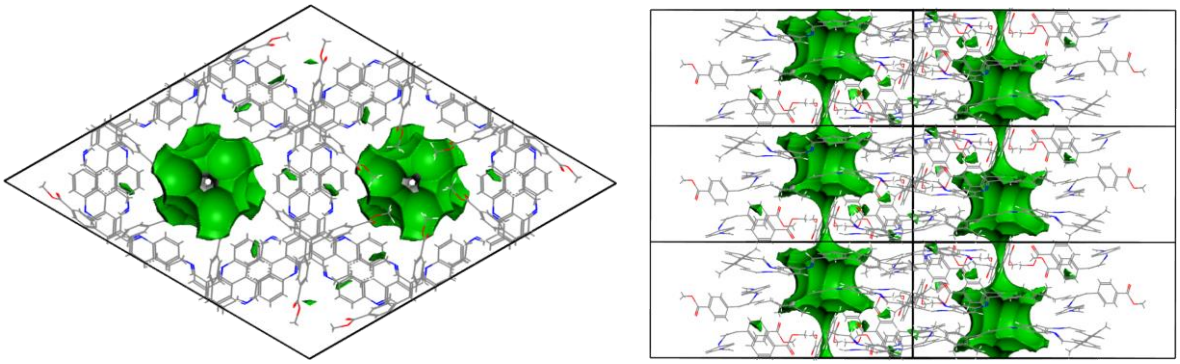

Figure S 4: Solvent accessible surfaces of the two central pores in the **4A2E**-PDA-COF with a 1.4 Å Probe radius viewed along the [001] direction (left) and the [110] direction (right). Symmetry equivalent pores at the unit cell boundary were omitted for clarity.

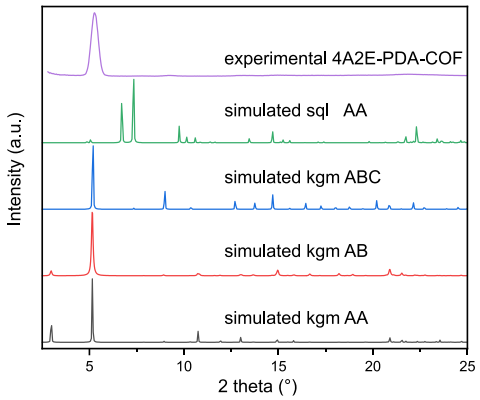

Figure S 5: PXRD comparison **4A2E**-PDA-COF with *sql* AA, *kgm* ABC, *kgm* AB and *kgm* AA stacking.

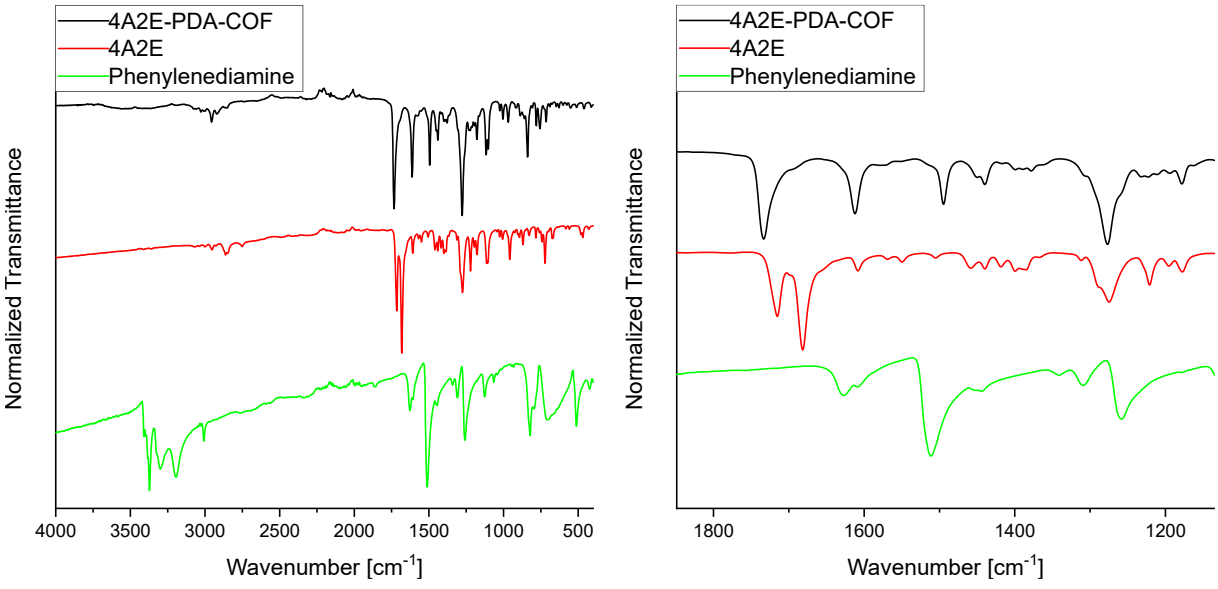

Figure S 6: IR of **4A2E**-PDA-COF (black), **4A2E** linker (red) and Phenylenediamine (green).

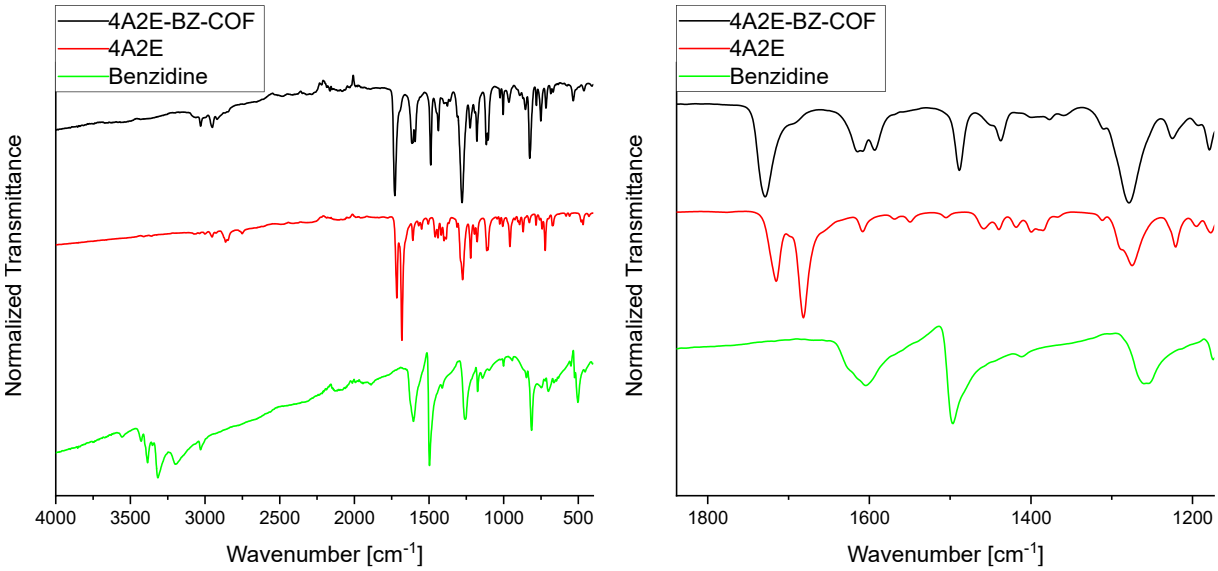

Figure S 7: IR spectra of **4A2E**-BZ-COF (black), **4A2E** linker (red) and Benzidine (green).

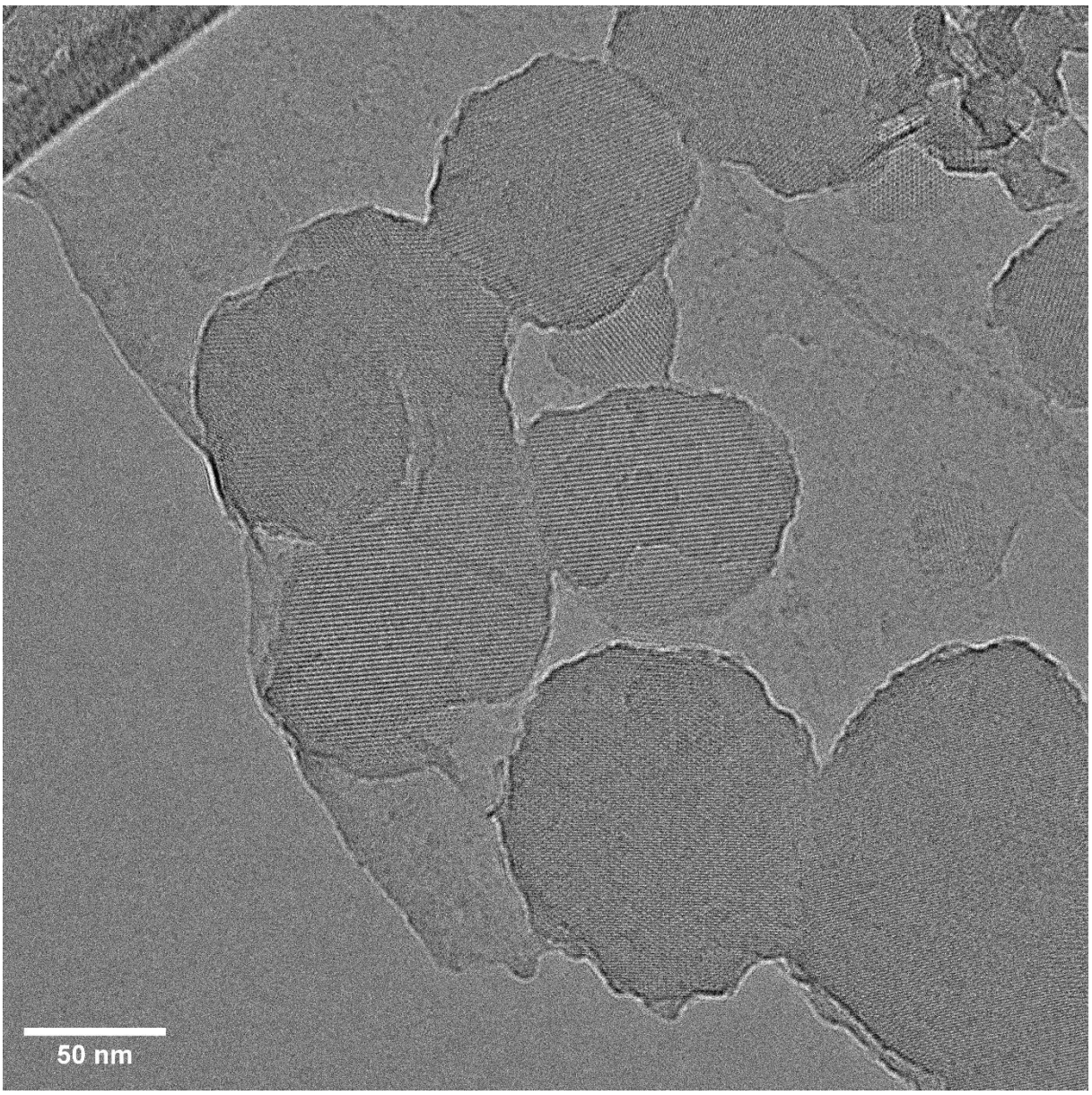

Figure S 8: Overview of particles of the **4A2E**-PDA-COF

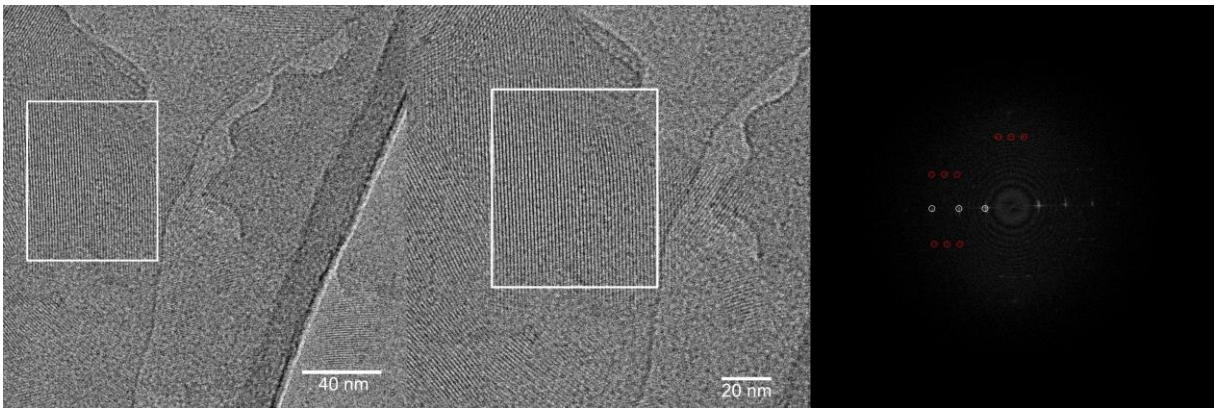

Figure S 9: TEM images of the **4A2E**-Bz-COF (left, middle) and the corresponding FFT image (right). The red circles in the FFT represent the superstructure.

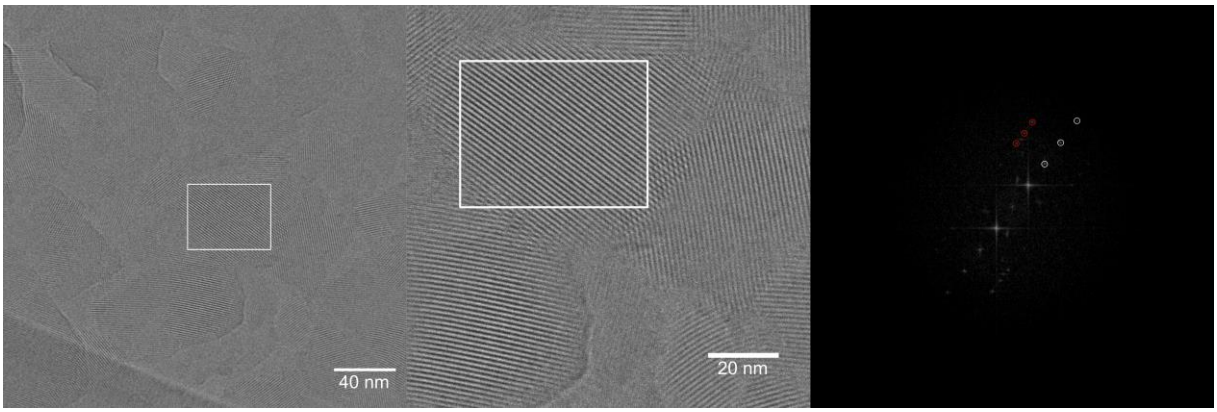

Figure S 10: TEM images of the **4A2E**-Bz-COF (left, middle) and the corresponding FFT image (right). The red circles in the FFT represent the superstructure.

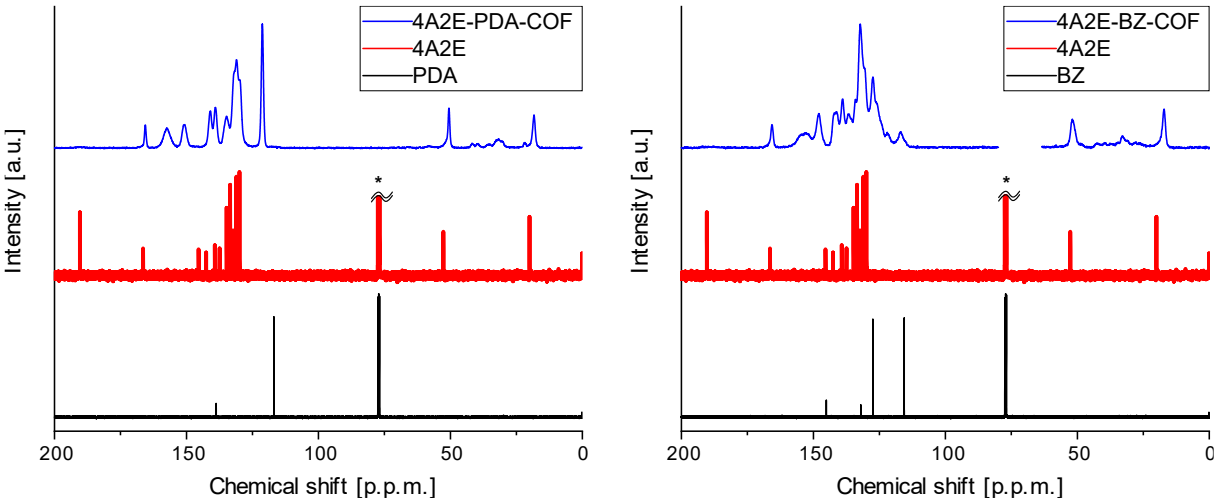

Figure S 11: Comparison of ssNMR of COFs (blue) with solution state NMR of **4A2E** (red) and diamine (black). **4A2E**-PDA-COF (left) **4A2E**-BZ_COF (right).

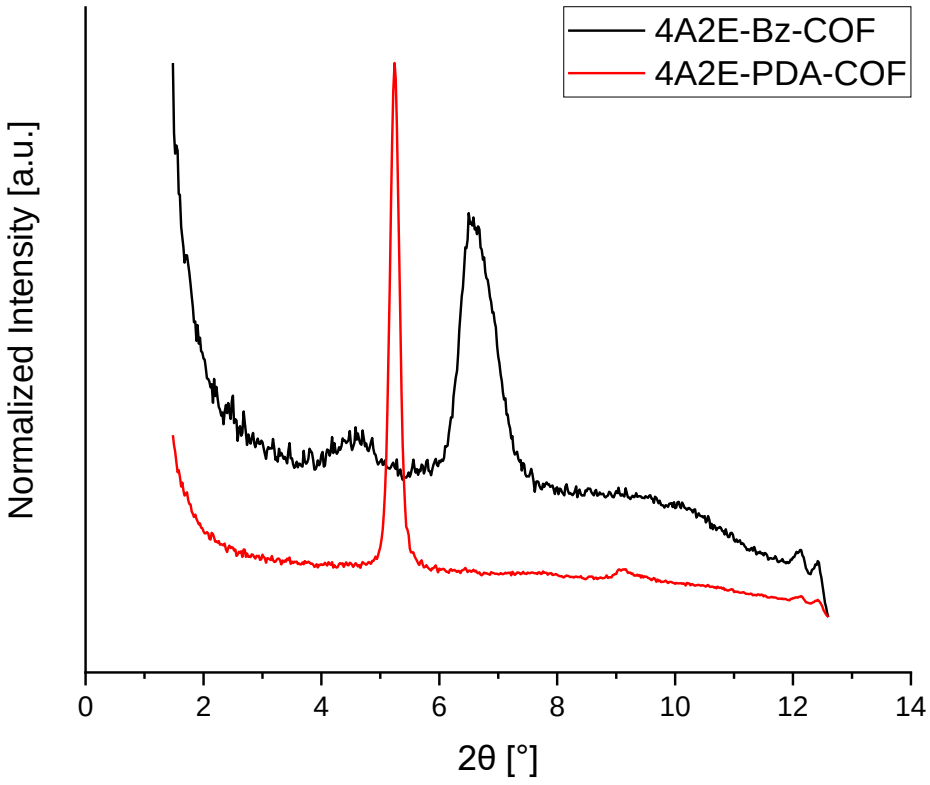

Figure S 12: PXRD measurement of the **4A2E**-PDA-COF and **4A2E**-Bz-COF in the small angle configuration.

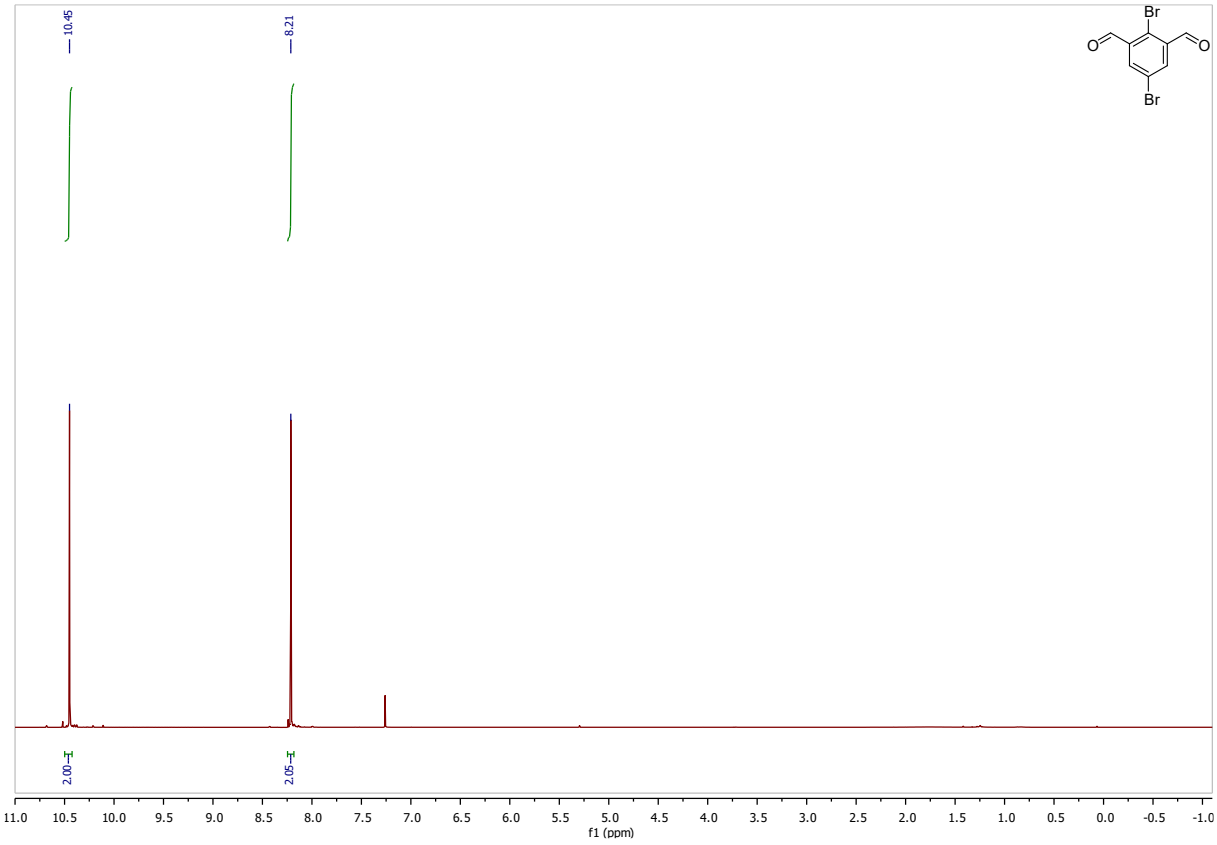

Figure S 13: ^{1}H NMR of 2,5-Dibromoisophthalaldehyde

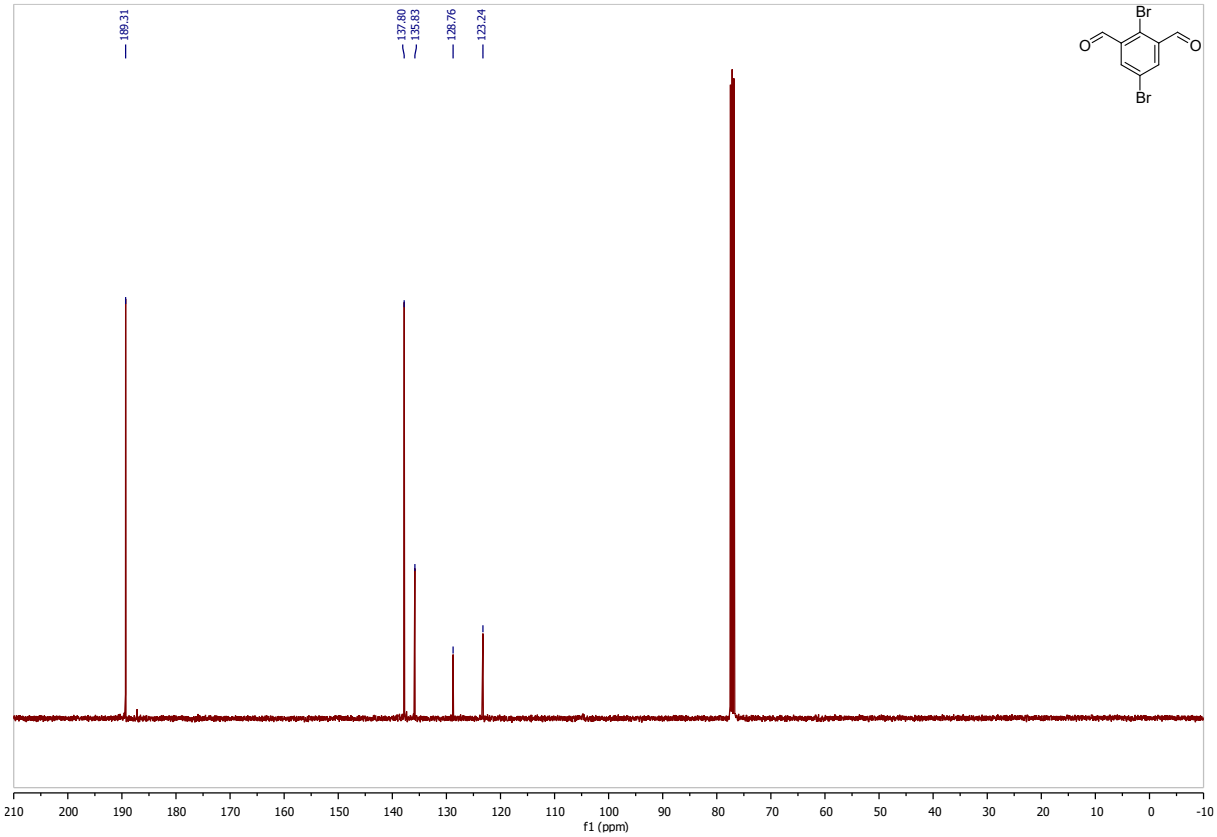

Figure S 14:[13]C NMR of 2,5-Dibromoisophthalaldehyde

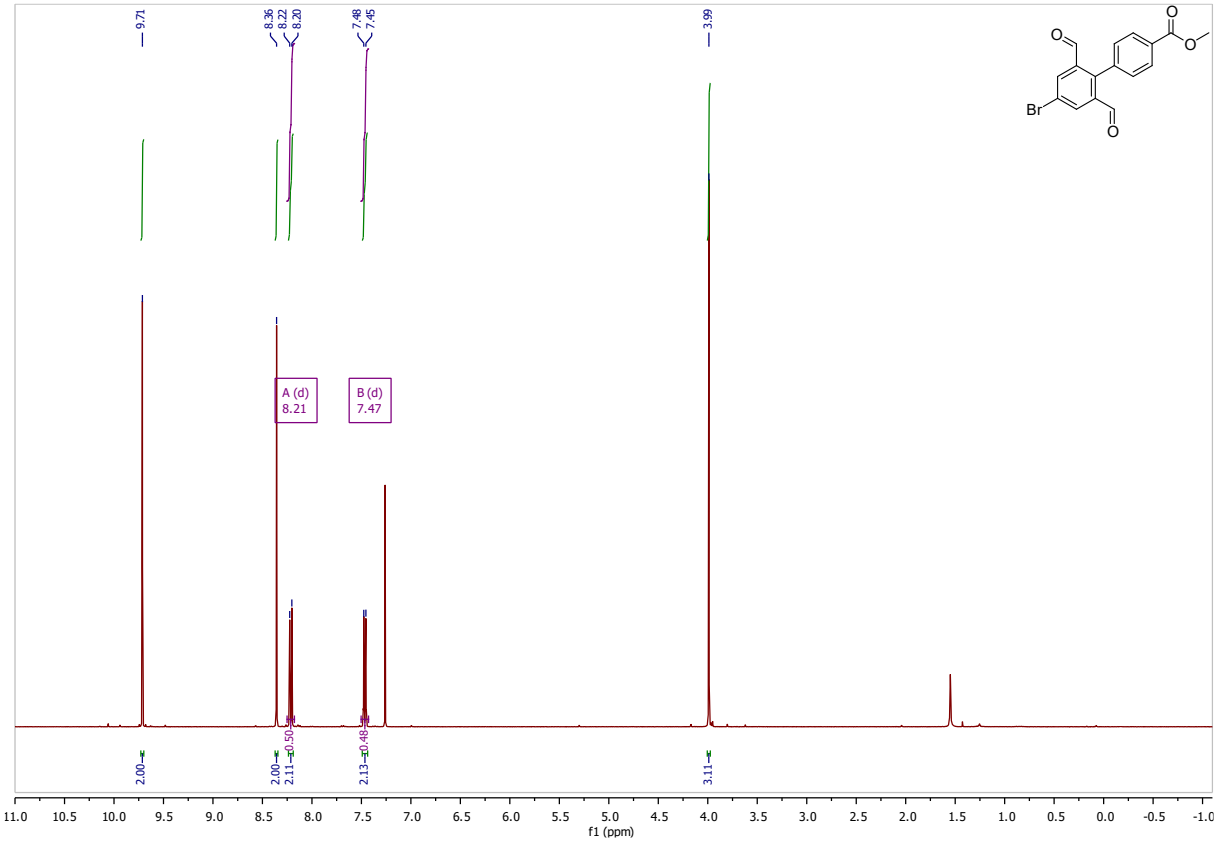

Figure S 15: [1]H NMR of Methyl 4'-bromo-2',6'-diformyl-[1,1'-biphenyl]-4-carboxylate

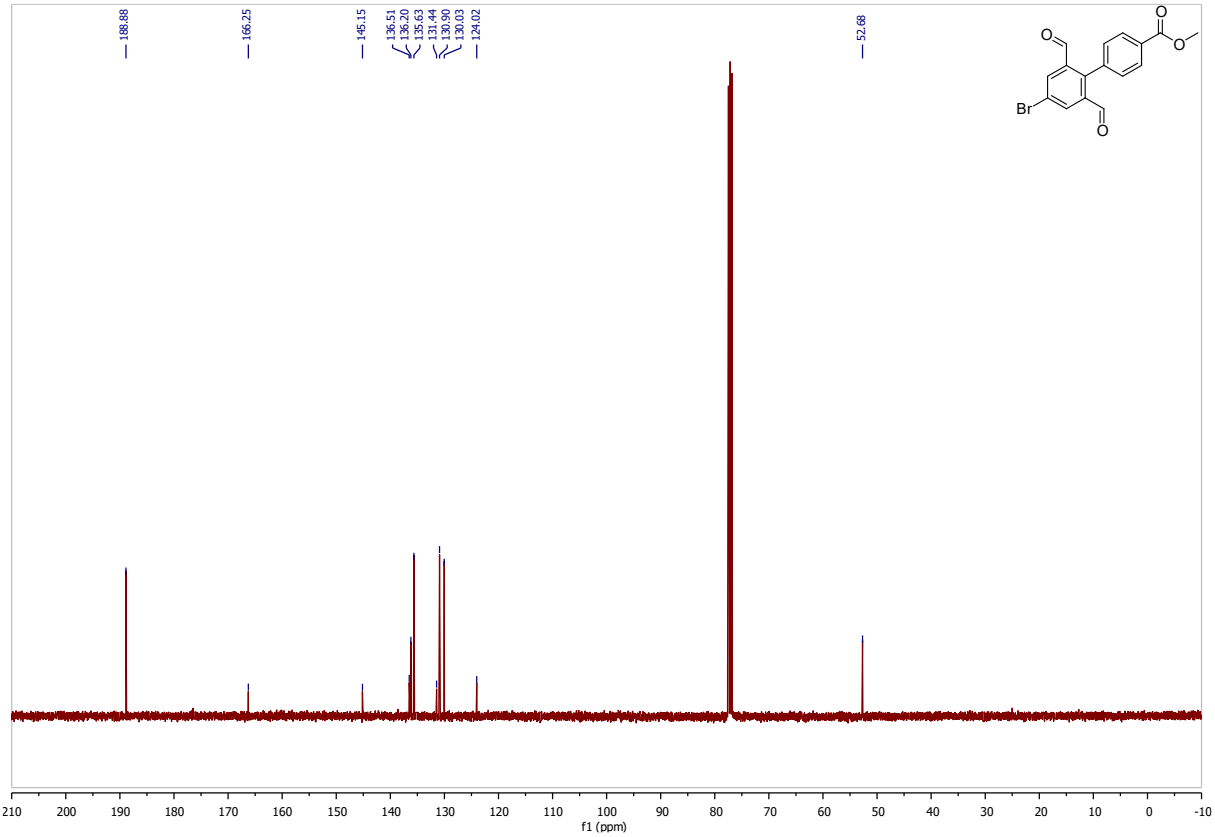

Figure S 16:[13]C NMR of Methyl 4'-bromo-2',6'-diformyl-[1,1'-biphenyl]-4-carboxylate

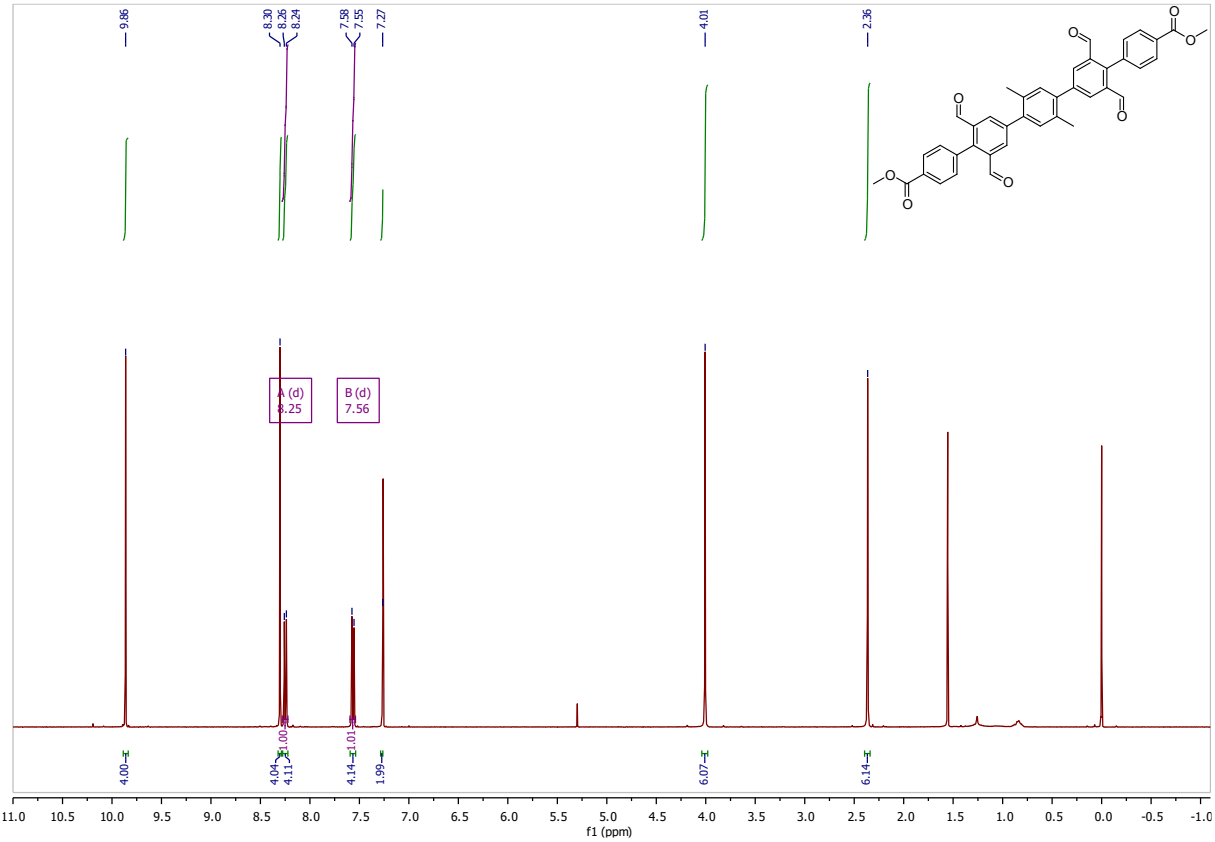

Figure S 17: [1]H NMR of **4A2E**

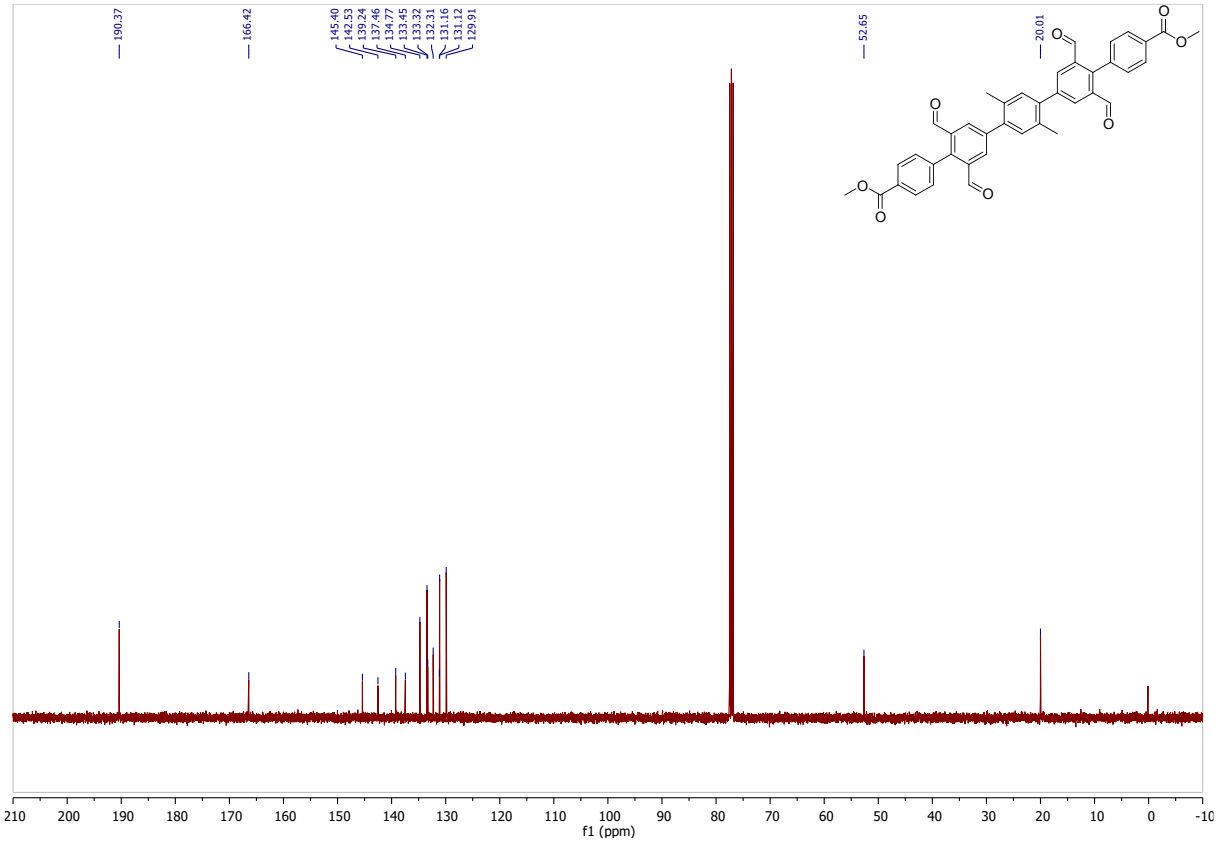

Figure S 18: ^{13}C NMR of **4A2E**

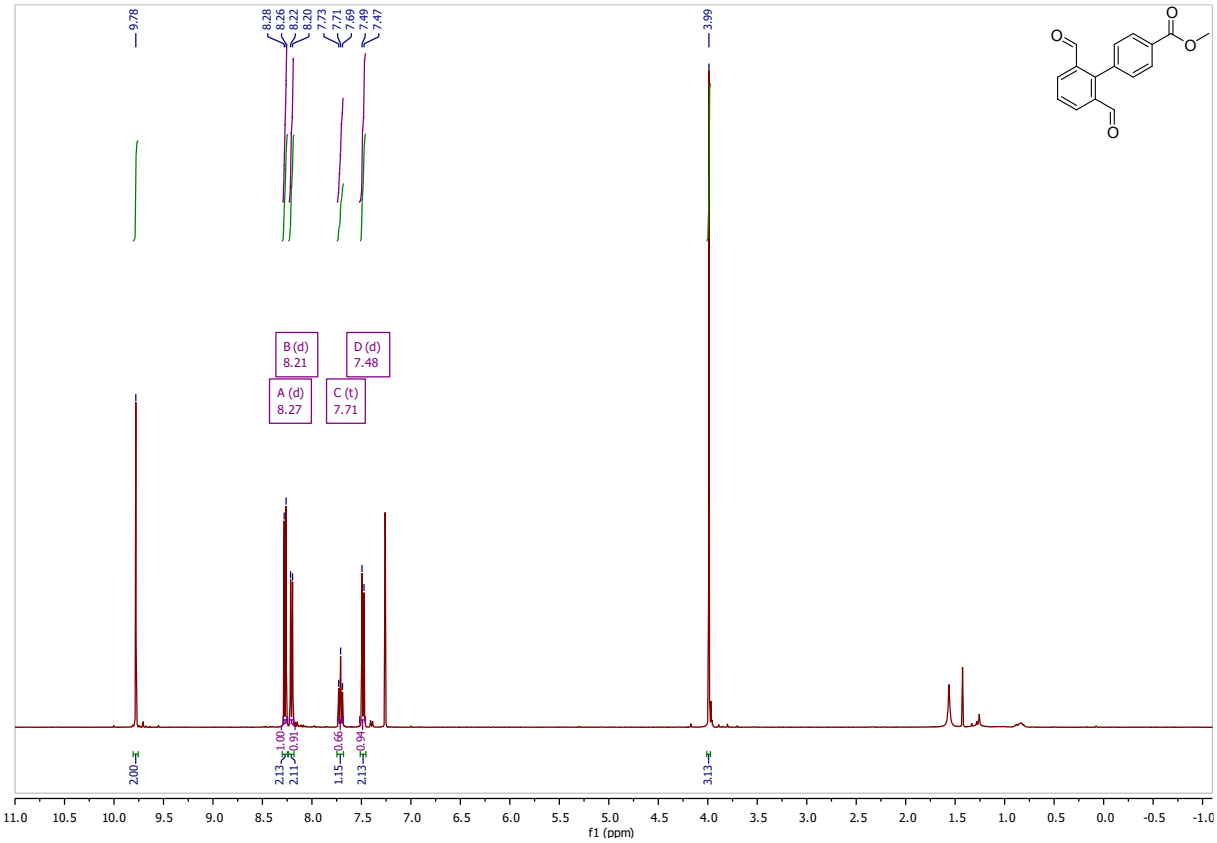

Figure S 19: ^{1}H NMR of Methyl 2',6'-diformyl-[1,1'-biphenyl]-4-carboxylate

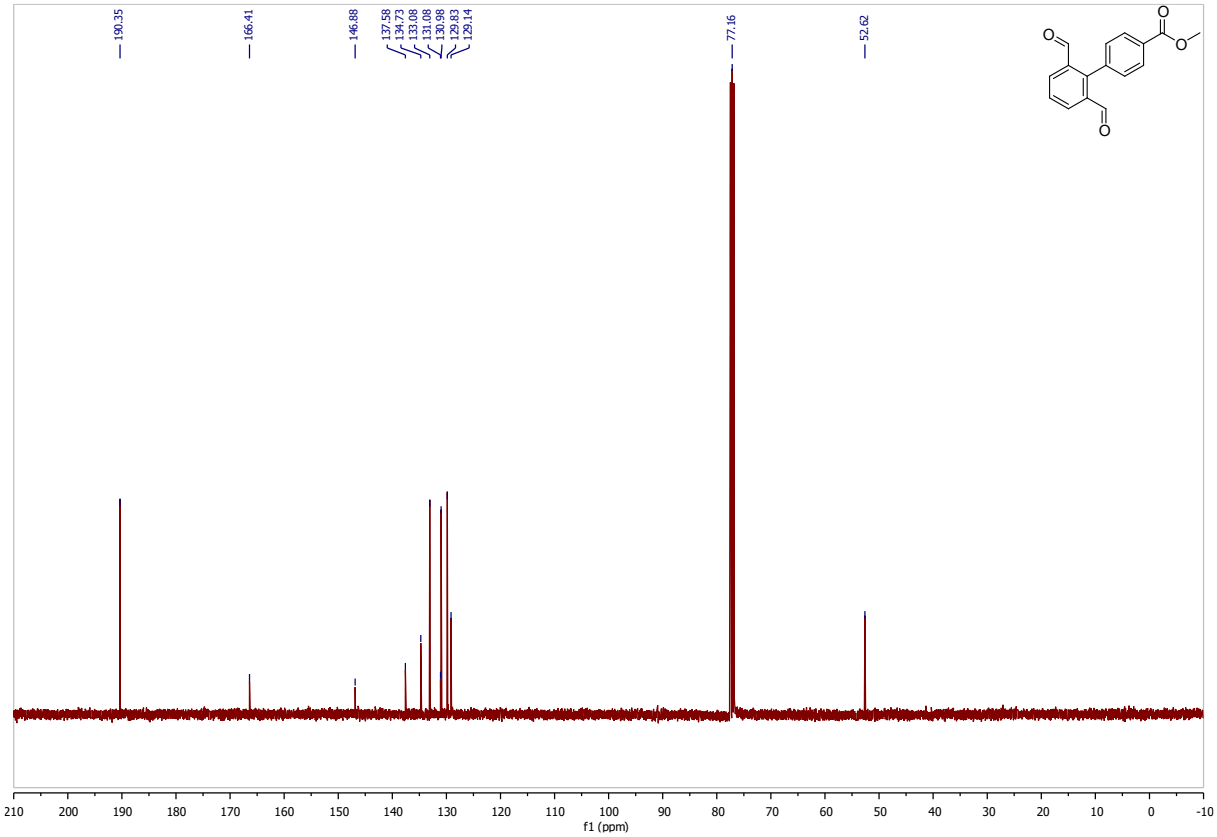

Figure S 20: ^{13}C NMR of Methyl 2',6'-diformyl-[1,1'-biphenyl]-4-carboxylate